Ponding Excess Water Mapping in Agricultural Areas in Hungary

Qiu Yun
March, 2017

SUPERVISORS:
1st Dr. Zoltán Vekerdy
2nd Ir. Arno van Lieshout

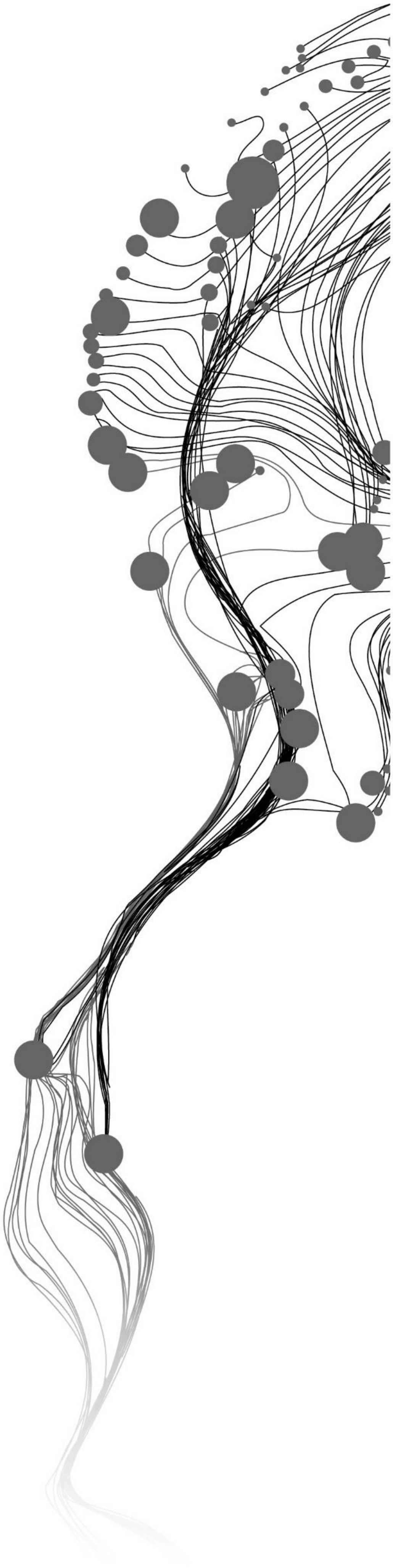

Ponding Excess Water Mapping in Agricultural Areas in Hungary

Qiu Yun
Enschede, The Netherlands, March, 2017

Thesis submitted to the Faculty of Geo-Information Science and Earth Observation of the University of Twente in partial fulfilment of the requirements for the degree of Master of Science in Geo-information Science and Earth Observation.
Specialization: Water Resource and Environment Management

SUPERVISORS:
1st Dr. Zoltán Vekerdy
2nd Ir. Arno van Lieshout

THESIS ASSESSMENT BOARD:
Dr. Ir. S. Salama (chairman)
Dr. Chen Shi (External Examiner, College of Resource Environment and Tourism, Capital Normal University, Beijing, China)
Dr. Zoltán Vekerdy
Ir. Arno van Lieshout

#ABSTRACT

Ponding excess water is a serious problem in Hungary since it causes a significant loss of agricultural production in damage in large rural regions. Ponding water damages the crop in the field which leads to a significant decrease of NDVI and crop growth. It is important to identify the location, spatial extension and severity of excess water inundation in agricultural areas. This study is done over northern region near Tisza River and South region near the city Szeged in Hungary. Remote sensing techniques especially microwave remote sensing can be used for mapping and quantitative estimating of ponding excess water inundation. Microwave remote sensing can monitor agricultural fields without the influence of cloud cover. Because of the improved revisit time and high resolution, the recently launched satellite, Sentinel-1, was used in this research. This study aims to map ponding excess water and assess its effects on crops with Sentinel-1 images, supported by field information in combination with other type of remote sensing products such as Sentinel-2 and multi spectral images derived from drones plus geospatial data such as DEM.

Backscatter, rainfall and soil moisture time series was used together for detecting the ponding water. Ponding water usually has low backscatter value (less than -14 dB). Polarization ratio can also be used to monitor the crop growth condition. Polarization ratio time series from Sentinel-1 share a good relationship with NDVI time series which derived from Sentinel-2. Specific soil texture affects the infiltration rate and leads to the occurrence of ponding water. Naturally low lying areas are more prone to ponding water.

According to the statistic of the mapping result based on images from October, 2015 to October, 2016 about 91.4 km^2 areas were affected by the ponding water over northern study area. 79.5 km^2 South study area was affected by the ponding water. For northern study area, most of ponding water stayed in the field during from January to February. For South study area, most of ponding water stays in the field from February to March.

Keywords: Ponding water, Sentinel-1, Sentinel-2, Agricultural field, backscatter time series analysis

ACKNOWLEDGEMENTS

I am grateful that I can have the opportunity to join the double master program between ITC and CNU. Much thanks for the cooperation between ITC and CNU which makes me have the opportunity to learn the advanced knowledge about geo-information science and earth observation in both China and the Netherlands.

I must also show my heartfelt thanks to my parents for their unconditional support, encourage and love.

Then I would like to express special gratitude to my supervisor Dr. Zoltan Vekerdy for the valuable advice, suggestions, patience guidance throughout the whole period of this research. You are always there (either on Skype or in your office) providing me help no matter if we have reservation or not. Many thanks for the field work you provided me. I learn a lot from it. I would also like to thank my second supervisor Ir. Arno van Lieshout for the advice, suggestion and comments to improve the thesis.

I would like to send my sincerely thanks for those people who provide me help during my field work in Hungary. Without your help and precious data, this thesis cannot be finished. Thanks Dr. Sándor Szalai, head of Water Management department of Szent István University, for his support and providing the opportunity to join the crew of the department. Thanks Dr. László Tolner for supporting the joint work with Edina and taking me into the team of the publication. Much thanks Edina Czakó-Gál and Pál Czakó for the warm-hearted welcome and the practical support, including transport and time during the fieldwork, as well as for sharing data of their farm. Thanks Prof. Erika Michéli for providing the brand new drone of the Soil Science and Agrochemistry Department, and Ádám Csorba, PhD Candidate, for his time and efforts in carrying out the drone flights in the northern area. I must also say thanks to Dr. István Waltner and János Grosz for providing me shelter in their office. János Grosz also helps me to trace the daily rainfall data for northern study area. I would also like to thank Prof. Dr. Gábor Mezősi, head of the Department of Physical Geography and Geo-informatics in University of Szeged, for providing resources including transport and time for the fieldwork. Big thanks Dr. Boudewijn van Leeuwen and his colleagues for carrying out drone flights and guiding us in the field in spite of the terrible weather.

Finally, I would like to say thanks to the friends I met in ITC. The happy time shared with you here is also the power which motivates me to complete my studies.

TABLE OF CONTENTS

LIST OF FIGURES

LIST OF TABLES

1. INTRODUCTION

1.1. Background

Ponding excess water is surplus water from excessive precipitation, snow melt or upwelling groundwater. It usually occurs on flat surfaces and results in temporary inundation because of insufficient evaporation, runoff and absorption capability of soil (Pásztor et al., 2014 & Leeuwen et al., 2013). Ponding excess water is regarded as a serious problem in several lowland European countries (Karoly, et al., 2013). More than 45% of Hungary's area is lowland which is threatened by ponding excess water inundation (Kuti et al., 2006). Figure 1 shows the inundation affected area in Hungary since 1935. It can be seen that the affected area can reach 400-600kha in some years. In 2016, there was about 100 kha area affected by ponding excess water.

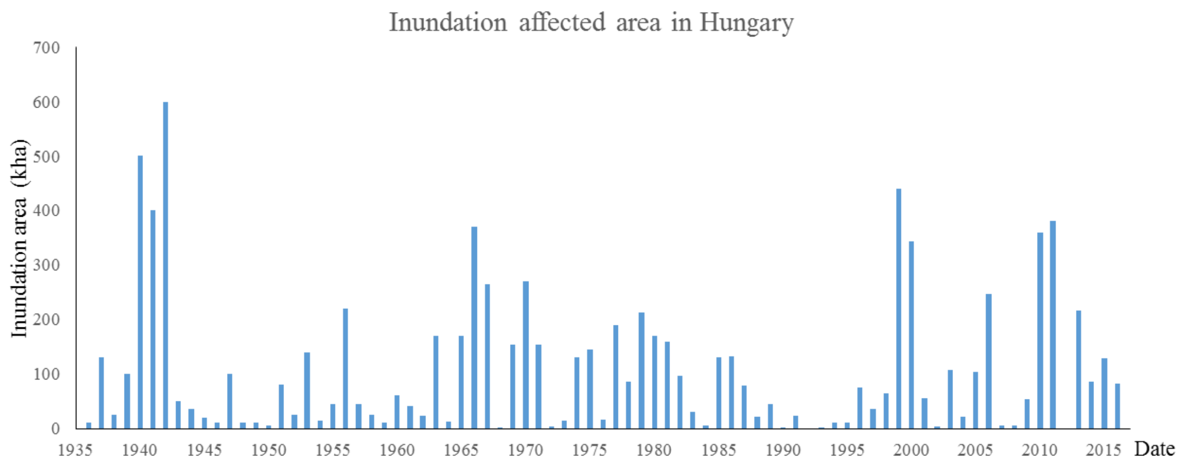

Figure 1 Inundation affected area in Hungary[1]

Ponding excess water can be regarded as a hazard for it can pose damage in agricultural regions (Pásztor et al., 2014). The main reason of the damage is that the ponding water blocks the uptake of oxygen and nutrient (Karoly et al., 2013). When ponding excess water occurs, the soil becomes saturated. It prevents root growth, leaf area expansion and photosynthesis (Ciampitti et al., 2015). The occurrence of ponding excess water prevents agricultural field activity such as ploughing, seeding and harvesting which affects the quantity and quality of agricultural products.

It is important to identify the location, spatial extension and severity of inland excess water inundation. Authorities can use this information to carry out preventive measures. Remote sensing techniques can be used for mapping and quantitative estimating of ponding excess water inundation (Leeuwen & Tobak, 2014). Either the remote sensing images from optical or microwave sensors can be used to monitor,

[1] from https://www.vizugy.hu/index.php?module=documents&programelemid=13, accessed 2017. January 5.)

forecast and assess the damage caused by the inundation (Jeyaseelan, 2003). However, the availability of suitable multi-spectral imagery is limited by cloud cover and heavy vegetation canopies (Xie, Sha, & Yu, 2008). Alternatively, microwaves can penetrate cloud cover and, in addition, the backscatter signature of water is distinctive compared to that of vegetation (Joyce et al., 2009). Synthetic Aperture Radar (SAR) offers the possibility to operate day and night which makes 24-hour flood monitoring available (Desnos et al., 2000). Therefore, SAR appears to be an ideal sensor for the detection of inundated areas, although the optical imagery is more straightforward in terms of interpretation of the signal.

The Sentinel-1A satellite of the European Space Agency (ESA) launched in 2014 and its twin satellite, the Sentinel-1B launched in 2016 can acquire SAR images. Compared with its predecessors such as ERS-1/2 SAR and ENVISAT ASAR, its revisit time and coverage are dramatically improved (Torres et al., 2012). The satellite carries a C-band SAR sensor which offers medium and high-resolution imagery in all weather conditions (ESA, 2016b). Those features make Sentinel-1 more suitable to acquire data over crop growing regions and map crop fields.

1.2. Research problem

Because of the flat topography, excessive precipitation, high groundwater table, insufficient evaporation and infiltration, Hungary faces the problem of ponding excess water which brings a huge loss of agricultural production. Remote sensing techniques have a large potential for mapping ponding excess water and for the quantitative estimation of its influence. Especially, Sentinel-1with its SAR sensor has a potential for mapping the extent of this hazardous phenomenon. Therefore, in this study, ponding excess water was analysed by this advanced satellite to assess its spatial and temporal distribution and provide essential information related to prevention and management.

1.3. Research objective

1.3.1. General objective

To map ponding excess water and assess its effects on crops with Sentinel-1 images, supported by field information and other remote sensing/geospatial data such as Sentinel-2 and drone images as well as DEM.

1.3.2. Specific objective

Three specific objectives are listed below to achieve the general objective of this research:

1) To identify ponding excess water by using multi-temporal Sentinel-1 images
2) To identify the land cover of agricultural areas by using multi-spectral images from Sentinel-2 data.
3) To assess the effects of ponding excess water on agricultural areas based on the time series analysis of SAR backscatter, rainfall, soil moisture and NDVI data.

1.4. Research questions

The following research questions are formulated to achieve the specific objectives:

1) How can inundation be identified by using Sentinel -1 data? (Specific objective 1)
2) How to identify agricultural fields by using multi-temporal NDVI features? (Specific objective 2)
3) How to classify the inundation area, permanent water bodies and map the ponding water in agricultural fields? (Specific objective 1)
4) How large area of crops is affected by inundation (Specific objective 3)
5) Which kinds of crop are vulnerable to the inundation? (Specific objective 3)

1.5. Novelty of the research

This research made it possible by the launch of a new generation of satellites which are suitable to monitor and map the areas affected by surface ponding excess water in agricultural fields and provide important information for preventive management actions. Sentinel-1 has not been used extensively to obtain data for mapping ponding excess water in Hungary. Most likely the Sentinel-1 images have a large potential for inundation monitoring, especially in the agricultural areas, but this has to be proven.

2. LITERATURE REVIEW

2.1. Review of ponding excess water mapping

Ponding excess water strongly influence the Great Hungarian Plain in Hungary, especially in agricultural fields (Mezosi, Bata, Meyer, Blanka, & Ladanyi, 2014). Agricultural fields as the most vulnerable areas require more accurate and reliable maps related to the hazard and occurrences of ponding excess water. In order to develop plans to reduce the impacts, several organizations in Hungary such as University of Szeged attempt to map ponding excess water. The first attempt to map the hazard with remote sensing dates back to the early 1980s. Then, more ponding excess water mapping was done on the north-eastern and southern regions of the Great Hungarian Plain (Bozán et al., 2008 & Pásztor et al., 2014).

With the development of remote sensing, satellite images have been used in mapping surface inundation for its higher efficiency and accuracy in comparison to in situ methods. Mid-resolution optical sensors, such as MODIS and Landsat TM can be used for monitoring ponding excess water (Guerschman et al., 2011). But, the optical sensor has its limitations. Inundations usually happen with heavy rainfall in combination with heavy cloud cover. The optical sensor cannot penetrate cloud cover to obtain effective data from the surface. Therefore, SAR is widely used later due to its all-weather, day and night coverage. High-resolution images from radar satellite such as COSMO-SkyMed, Radarsat-2 and TerraSAR-X can be used for detecting inundated areas (Pierdicca et al., 2009; Hoque et al., 2011 & Gstaiger et al., 2012). Compared to these high spatial resolution sensors, the temporal resolution of Sentinel-1 is higher (Torres et al., 2012). A higher temporal resolution provides more frequent mapping possibility.

Sentinel-1A was launched on 3th April 2014 and Sentinel-1B was launched on 25th 2016 (ESA, 2016b). Their sensors have four standard modes: a) Strip Map Mode has an 80 km swath and 5x5m spatial resolution. b) Interferometric Wide Swath Mode has 250 km swath and 5x20m spatial resolution. c) Extra-wide Swath Mode has 400 km swath and 25x100m spatial resolution. d) Wave Mode has a low data rate and 5x20m spatial resolution. For each mode, it also has a selectable dual polarisation which can meet different monitoring and mapping demands (Attema et al., 2007). Sentinel-1 has been used, for example, in flood monitoring and mapping (Boni et al., 2016; Twele et al., 2016 & Schlaffer et al., 2015). The first Sentinel-1 map was used for monitoring a serious flood in Namibia (ESA, 2016b).

2.2. Review of Time series analysis

The temporal characteristics of a series data can be found by time series analysis. It is a very common method to monitor crop and surface inundation. Wardlow et al. (2007) used time series analysis of NDVI calculated using MODIS data for a large-area for crop mapping in the U.S. Central Great Plain. They found different crop shows different temporal patterns on the time series which reflects its crop phenology. Ho et al. (2011) compared the time series of NDVI acquired from MODIS with the time series of soil moisture, vegetation water content, and soil/canopy temperatures acquired from AMSR-E over the Cooper Creek catchment. The time series analysis was used for identifying the presence of surface water from before to after a single flood event and they found it is a very ideal method for observing the crop loss from a hydrology event. Skakun (2012) proposed time series analysis of Landsat-5/7 data acquired in the period of 2000 to 2010 for flood hazard mapping in Namibia and found that this method can be used even though the hydrological model is complicated and lacks some data. Moran et al. (2012) analysed the time series of backscatter coefficient and found it can provide relevant information of soil conditions and crop growth stage in Barrax, Spain.

2.3. Water identification in SAR images

The roughness and dielectric properties of the surface affects the backscatter coefficient (Velde, 2010). Different types of surface have different backscatter coefficients ($\sigma°$). Water bodies can be regarded as a flat surface on which specular reflection happens (Figure 2, a). The incidence angle (θ_i) is equal to scattering angle (θ_s) which makes the entire incidence wave reflect in specular direction. So, water bodies usually produce a low backscatter coefficient response and appear dark in the SAR image. Rougher surfaces can scatter the incident microwave and generate a larger backscatter response (Figure 2, b), that makes a bright tone in the SAR images (Velde, 2010). Furthermore, wet soil has a larger dielectric constant than the same surface with a lower moisture content, that results in higher backscattering and appears also bright in SAR images (Velde, 2010). All these characteristics can be used for ponding excess water identification.

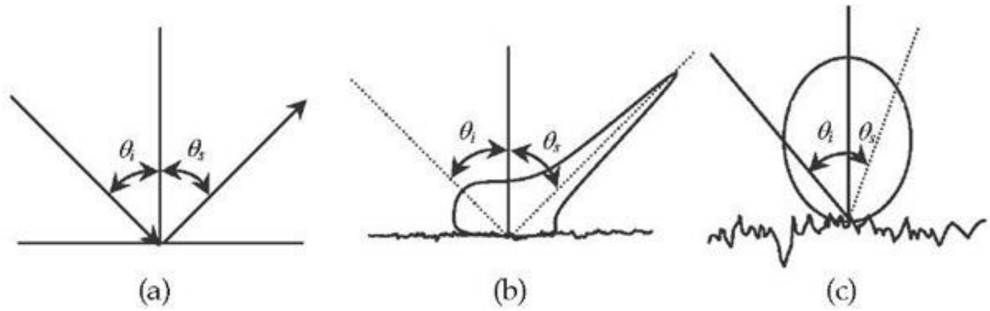

Figure 2 Different scattering patterns under different surface roughness condition specular (a), slightly rough (b), very rough(c)[2].

At present, SAR image based water extraction methods mainly include: extraction based on texture information, combined with terrain auxiliary information, independent component analysis and threshold segmentation (LingFang Zeng, Lin Li, 2015). The widely used threshold segmentation method has a simple principle. This method is based on the characteristics of water body in SAR image. A corresponding threshold value is set to separate water body and background respectively. Pierdicca et al. (2009), Pulvirenti et al. (2011), LingFang Zeng et al. (2015) and Twele et al. (2016) used this method to extract inundation area.

[2] http://what-when-how.com/electromagnetic-waves/models-for-scattering-from-rough-surfaces-electromagnetic-waves-part-1/

2.4. Surface scattering in agricultural fields

Radar backscattering from agricultural fields includes the volume scattering in the canopy, surface scattering from ground surface and multiple interactions between vegetation and ground surface. Equation 1 shows the basic conceptual assumptions. The backscatter (in dB or in m^2 m^{-2}) from the whole surface (σ°) can be considered as the sum of contribution of vegetation (σ°_{veg}), soil (σ°_{soil}) which is attenuated by the canopy and soil- vegetation pathway ($\sigma^\circ_{veg+soil}$) (Velde, 2010).

$$\sigma^\circ = \sigma^\circ_{veg} + \sigma^\circ_{veg+soil} + \gamma^2 \sigma^\circ_{soil} \qquad \text{Equation 1}$$

where $\gamma^2$is the two-way vegetation transmissivity

In agricultural areas, the analysis of surface scattering should consider the contribution of vegetation backscatter and soil moisture absorption (Bindlish & Barros, 2001). Different soil and vegetation conditions have different relationships between the backscatter coefficient and the moisture content of the soil (Moran et al., 2012). The contribution of vegetation backscatter includes the volume scattering produced by vegetation and the attenuation effect of soil on the backscattering, according to the Radiative Transfer Theory (Paloscia et al., 2013). The relationship between backscatter and canopy can be estimated by using NDVI value and polarization ratio (Paloscia et al., 2013). Bindlish & Barros (2001) found there is a regression relationship between backscatter coefficient and NDVI, especially in case of cross polarization where polarization ratio and NDVI have a higher correlation coefficient. Similar findings were also got by Paloscia et al. (2013). They found a regression relationship between polarization ratio and NDVI and found that the polarization ratio can also exhibit a rather good sensitivity to vegetation cover. As for the contribution of soil moisture, it is proved that there is a simple linear relationship between the backscatter signal and the soil surface volumetric moisture (Zribi, Baghdadi, Holah, & Fafin, 2005). As shown by Equation 2.

$$\sigma^\circ(dB) = a * W_s(\%) + b \qquad \text{Equation 2}$$

where $\sigma^\circ(dB)$ is the backscatter in dB unit; a, b are coefficients; $W_s(\%)$ is the soil surface volumetric moisture

3. STUDY AREA

3.1. Location

This research was carried out in two study areas. The location of the two study area shows in Figure 3 (a). One of them is the agricultural region close to the Tisza Lake on the north of Hungary (Figure 3, b). This study area (47.8°N~47.6°N, 20.2°E~20.7°E) is located on the south-eastern edge of Heves county. This area is the lowest part of the county, at about 100-130 metres elevation above sea level. The second study area (46.4°N~46.2°N, 20.0°E~20.5°E) is the agricultural region near the city of Szeged located at the south of Hungary (Figure 3, c). Five test sites were chosen on the northern study area. Four test sites were chosen in the southern study area. The location of these test sites are shown in Figure 3 (b, c)

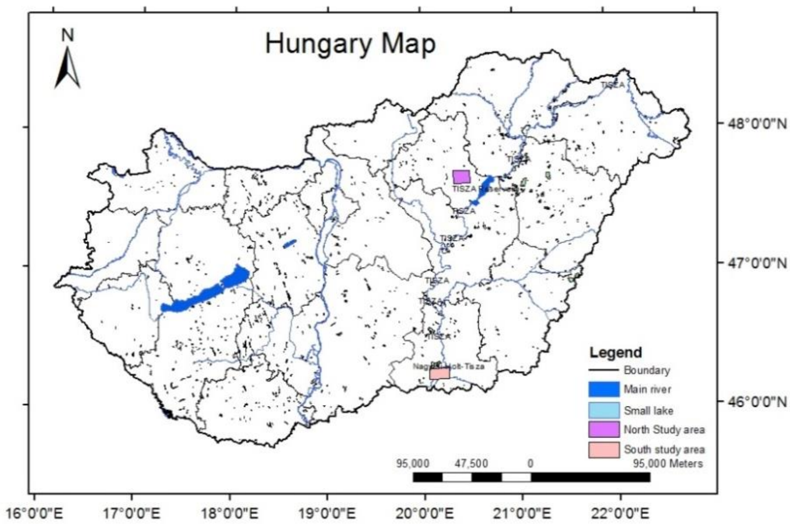

(a)

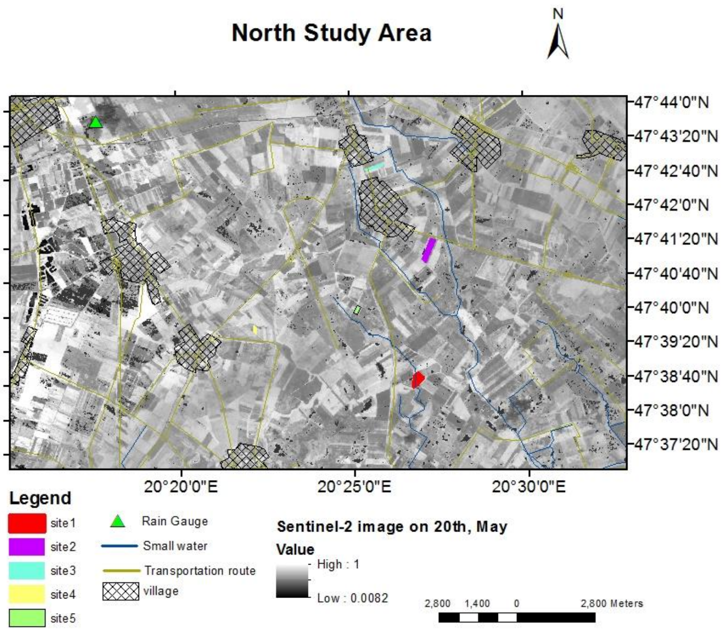

(b)

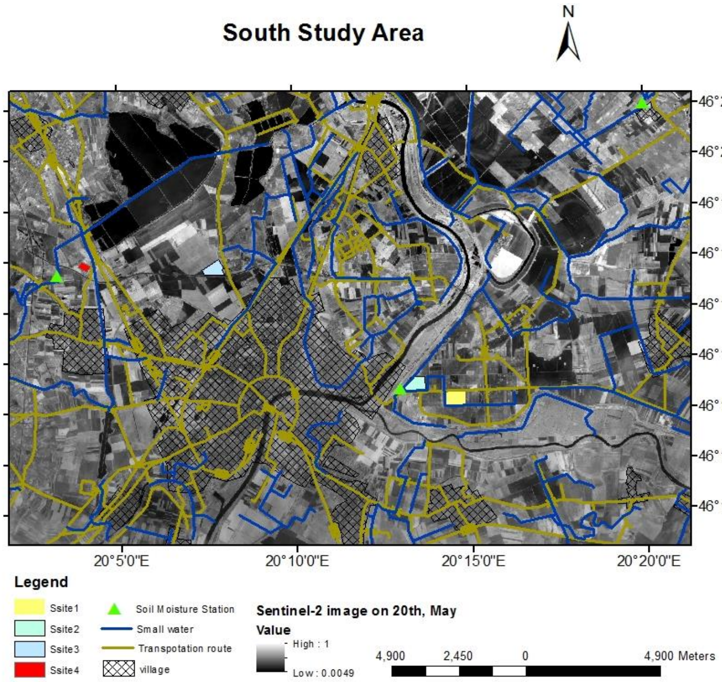

(c)

Figure 3 the location of the study area (a) and the test sites map on northern study area (a) and southern study area (c)

3.2. Climate

In Hungary, the annual average temperature is between 10 ℃ and 11 ℃ and the annual average precipitation is 500-800 mm (Mezosi et al., 2014). Monthly mean precipitation and relative humidity of Hungary are shown in Figure 4. Most precipitation falls between May and August. But at the same time, potential evaporation is high in this period. So, the ponding access water usually does not appear during this period because of the high evaporation. However, from November to March, the precipitation amount is not high, and combines with low potential evaporation. When there is an excessive precipitation, ponding excess water usually occurs during this period due to the low evaporation.

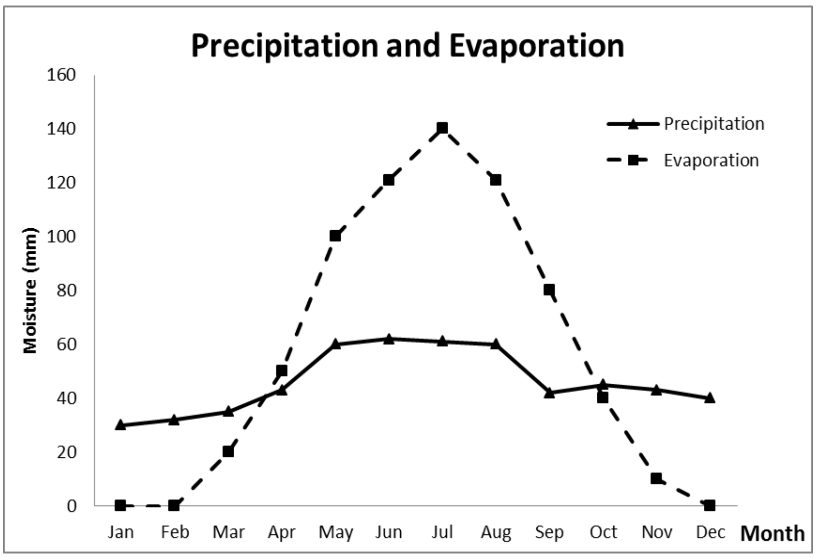

Figure 4 Monthly mean precipitations and evaporation of Hungary

3.3. Topography and land cover

Both the northern and the southern study areas are mainly farmlands. The main agricultural production of these regions is alfalfa, rapeseed and wheat (Appendix 1). In the regions prone to the accumulation of ponding excess water, soils have a heavier texture ranging from clays to clayey loams. The terrain of both test area is flat (Mikl, 2011). It results in the high-frequency occurrence of ponding excess water in spring when there is an excessive precipitation or melting of snow.

3.4. Field work and data collection

A field work was conducted from 29th September to 16th October for collecting the necessary field data. The following tasks were completed during the field work:

- **Test area selection**

Test sites were selected with optimal data sets to identify surface inundation areas based on land cover map, drone images and in-situ identification.

- **Reconnaissance**

Observing landscape, crop type, the location of inundation and agricultural activities in the study area.

- **Drone survey over test sites**

Observing terrain details such as crop type and agricultural activities in the study area. DEM (digital elevation model) was also extracted from the aerial photos.

- **In-situ mapping and soil moisture measurements of inundated area**

The outline of the water area was measured and recorded by using GPS. The in-situ soil moisture was measured over both inundation areas and non-inundation areas by soil moisture sensor.

- **Archive data collection**

The required archive data such as rainfall and soil moisture time series, crop information were also collected during the field work.

3.4.1. Measurement device

Three devices used in the field work are showed in Figure 5. The coordinates of inundated areas and non-inundated areas were measured using the Gamin eTrex 30X GPS. The soil moisture of northern test sites 1, 3 and 5 was measured in situ using the DELTA-T Theta soil moisture sensor (HH1 Type). A DJI Phantom4 drone was also used for mapping selected areas. Aerial RGB photos were taken over test sites 1, 5 in the north and test site 4 in the southern test areas. In the north, there was no possibility of measuring high precision tie points, so the created DEM had an absolute elevation error more than 1 m. In the south, nine control points were chosen and 200 aerial photos were taken from a relative flying height of 90m (Figure 6). The photos were mosaicked, and then a DEM data was extracted resulting in a nominal vertical accuracy less than 10 cm.

（a）

（b）

（c）

Figure 5 the measurement device used in field work soil moisture sensor (a), GPS (b) and Drone (c)

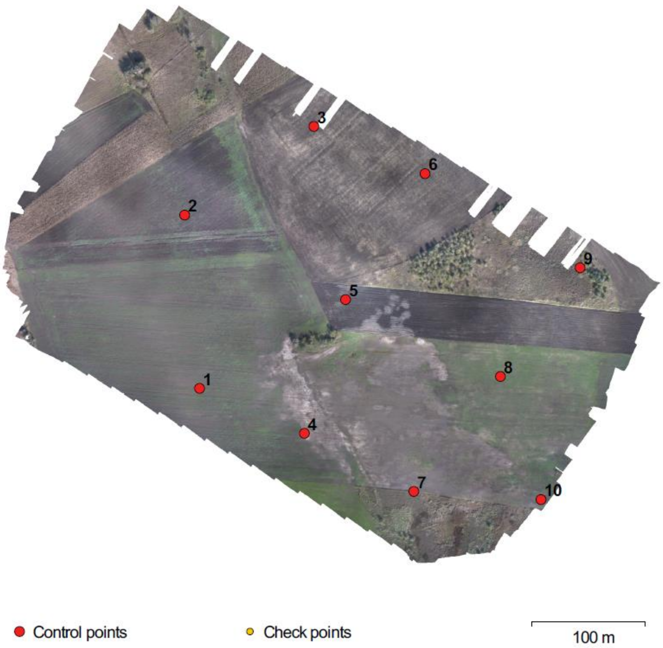

Figure 6 Ground control point locations used over South site 4

3.4.2. Description of the observed test sites

All the 9 test sites were visited during the field work. The farmer showed the area which is often affected by the inundation and provided the soil moisture and crop information over the sites (Appendix 1). The landscape and description about test sites are showed in Table 1.

Table 1 Description of test sites

	Test Site	Photo of the field	Description
Northern study area	Test site 1		This part of area (N47°38.751', E20°26.852') does not affected by the ponding water. The area is covered by thick alfalfa. The height of alfalfa is nearly half meters.
			This part of area (N47°38.724', E20°26.764') often affected by the ponding water. The crop is not tall and thick than the crops in non-inundation area.
	Test site 2		From the left side of the picture, it is easily seen that this area (N47°41.204', E20°27.086') is nearly bare. It results from the influence of ponding water.
	Test site 3		It is the highest elevation part (N47°42.765', E20°25.537') of this test site. The area is covered by dense rapeseed.
			The terrain of this area (N47°42.840', E20°25.870') is quite low. Because of the low terrain, the ponding water often happens here which results in the low vegetation covered situation.

<table>
<tr><td rowspan="4"></td><td rowspan="2">Test site 4</td><td></td><td>The farmer said the land cover was rapeseed before. This site does not affected by ponding water.</td></tr>
<tr><td></td><td>This field (N47°40.056', E20°22.417') is near site 4. Winter wheat is going to be planted on this field. This area is usually affected by the ponding water.</td></tr>
<tr><td rowspan="2">Test site 5</td><td></td><td>The farmer said this area isn’t affected by ponding water (N47°39.993', E20°25.051'). The alfalfa grows well here.</td></tr>
<tr><td></td><td>The farmer said this part (N47°40.036', E20°25.101') usually affected by the ponding water. The alfalfa here is seriously damaged by the inundation compared with the crop in non- inundation area.</td></tr>
<tr><td>Southern study area</td><td>Test site 1</td><td colspan="2">The field became muddy because of the heavy rain. The measurement could not be carried out in the field. The field was ploughed. There was no crop cover on the field.</td></tr>
</table>

	Test site 2		Drone was test over this test site but the quality of the aerial photo is not very good because of the bad weather. The field was ploughed. There was no crop covering the field. There is a petrol collection platform in the field.
	Test site 3	The field became muddy because of the heavy rain. The measurement could not be carried out in the field. The field was ploughed. There was no crop covering the field.	
	Test site 4		The field is covered by rapeseed. There was a very heavy rainfall. The ponding water started to accumulate during the our visit.

3.4.3. Rainfall data

Daily rainfall data from September 2015 to September 2016 was collected. For northern study area, the rainfall data was collected from a website called Metnet[3]. The meteorological station is in Heves near the northern study area shown in Figure 3 (b). For Southern area, all the rainfall data was collected from local meteorology stations related to an earlier project of the University of Szeged. The daily rainfall data from HU03 Tápé station and HU05 Kiskundorozsma stations were used for this study (the location shown in Figure 3, c).

3.4.4. Soil moisture data

The change of soil moisture content can result in the change of backscatter (Velde, 2010). In order to study the relation between soil moisture data and backscatter, in-situ soil moisture was collected. For northern study area, the soil moisture is collected at 15 cm depth in the framework of an Msc study submitted to the Szent István University, by Edina Czakó-Gál. The soil moisture measurement was carried on test site 5 from 23rd April, 2016 to 22nd July, 2016. For southern study area, the soil moisture data was measured at 5 cm depth from 7th Octorber, 2015 to 20th October, 2016. The soil moisture data of southern study area was also collected from local meteorology stations related to an earlier project of the University of Szeged. The soil moisture data from HU03 Tápé station and HU05 Kiskundorozsma

[3] https://www.metnet.hu/

stations were used for this study(the location shown in Figure 3, c). Soil moisture data was collected and used as a reference for the analysis of SAR data in mapping the surface inundation.

4. METHODOLOGY AND DATA

The flowchart (Figure 7) shows the overall methodology used in the research. The first step was the pre-processing of the satellite data. The backscatter coefficient maps were obtained after pre-processing. Then, the polarization ratio $(\frac{\sigma^{\circ}VH}{\sigma^{\circ}VV})$ was calculated. Next, statistical analysis of the backscatter was done over inundated areas and non-inundated areas. Several test sites were chosen for the analysis. Later, backscatter time series analysis was done together with other field work data such as rainfall and soil moisture data. Time series plots were used to demonstrate how these data change over time. NDVI was calculated from both Sentinel-2 and Landsat 8 images after atmosphere correction. Time series analysis of NDVI values together with crop height and polarization time series was used for displaying the crop condition and estimating the crop loss. The nine test sites were used to identify the characterizations of ponding water inundation. Then, a backscatter threshold was obtained for mapping the distribution of ponding water.

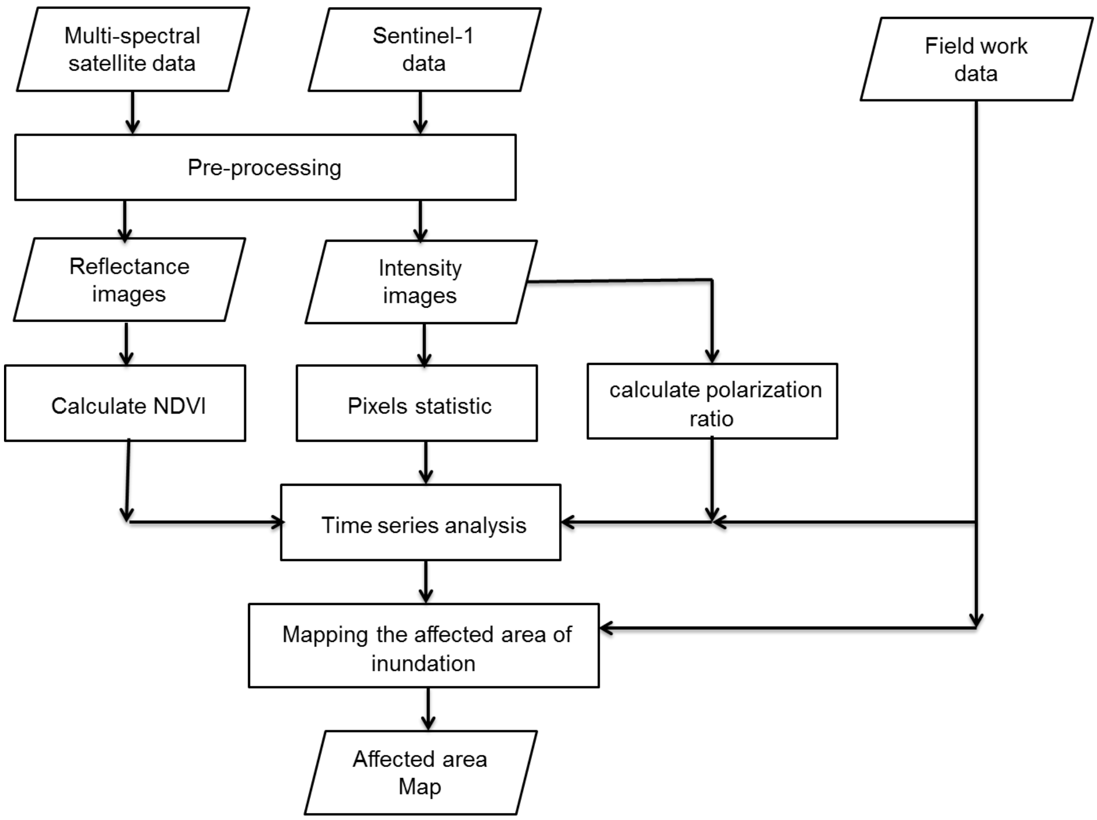

Figure 7 Methodology flow chart

4.1. Satellite Data

4.1.1. Sentinel-1

Level-1 Ground Range Detected (GRD) Sentinel-1A C-band (5.405GHz) data was used in this research. Interferometric Wide swath (IW) Mode was chosen. It has a 250 km swath with 5x20 m spatial resolution and burst synchronisation for interferometry (Attema et al., 2007). VV+HV polarization was used to provide ground surface information. Sentinel-1A data from September 2015 to September 2016 was collected through the ESA Scientific Data Hub[4]. There were 59 Sentinel-1A images used for northern study area and 58 Sentinel-1A images were used for southern study area. The interval of the images is alternatingly 5 or 7 days. In order to compare with a drone image, a Sentinel-1B image on 28th, October, 2016 was also used in this study.

4.1.2. Multi-spectral images

Level-1c Sentinel-2 data and Landsat 8 data from September 2015 to September 2016 with minimal cloud cover was collected. The research focused on the Sentinel-2 images, and Landsat 8 data was used as supplement. Sentinel-2 data was collected from the *ESA Scientific Data Hub*, whilst Landsat 8 was downloaded from *Satellite Search*[5]. The Semi-Automatic Classification Plugin in QGIS was used for downloading these 2 data. Sentinel-2 data has a wide swath, high resolution and a high revisit time of 5 days at the Equator. It can monitor the vegetation change during growing season because of these advantages (ESA, 2016). It has multi-spectral data with 13 bands in the visible, near infrared, and short wave infrared part of the spectrum. Visible (VIS) and Near-Infra-Red (NIR) bands was used for NDVI calculation (Ho et al., 2011). The VIS and NIR bands of Sentinel-2 data has a spatial resolution of 10 m. Landsat 8 has 8 bands and NIR bands were used to calculate the NDVI. The spatial resolution of these 2 bands is 30m. More details of Sentinel-2 data and Landsat 8 data are showed in the Appendix 2 (ITC, 2016).

4.2. Pre-processing

For SAR images, the purpose of pre-processing is the reduction of the distortions, degradations and noise (Frulla et al., 1998). The pre-processing phase of Sentinel-1 data includes creating subsets of the test areas, radiometric calibration, terrain correction, view angle correction and speckle filtering. All the Sentinel-1 images also need to be converted from the intensity unit ($m^2\ m^{-2}$) to the decibel unit (dB). The conversion is based on the Equation 3.

$$\sigma^{\circ}(dB) = 10 log_{10}\sigma^{\circ} \qquad \text{Equation 3}$$

Where σ° is the linear backscatter coefficient.

SNAP software was used for this stage. For Sentinel-2 and Landsat 8 images, the pre-processing step included atmospheric correction.

[4] https://scihub.copernicus.eu/dhus/#/home.

[5] https://remotepixel.ca/projects/satellitesearch.html.

4.2.1. Radiometric calibration of SAR images

The purpose of radiometric correction is adjusting possible temporal changes of the antenna gain and converting amplitude digital numbers into backscattering coefficients (Frulla et al., 1998). The calibration is done based on the Equation 4 and 5. These Equations show the radar measurement principle (Velde, 2010).

$$P_r = \frac{P_t G_t A}{(4\pi R^2)^2}\sigma \qquad \text{Equation 4}$$

$$\sigma^{\circ} = \frac{<\sigma>}{A_0} \qquad \text{Equation 5}$$

where P_r is received power [W], P_t is transmitted power [W], G_t is transmitter power gain [-], A is effective area of the antenna [m^2], R is distance between the target and the radar [m], σ is scattering cross section of a target [-], A_0 is the illuminated area [m^2] and σ° is referred to as the backscattering coefficient [m^2 m^{-2} or decibels, dB].

4.2.2. Geometric correction of SAR images

Irregularities of the surface topography cause distortion in the SAR images such as foreshortening, layover and shadow. It is necessary to apply geometric corrections to project images to the proper geometric basis. The Range-Doppler Terrain Correction is applied to the SAR data after the radiometric calibration by using SNAP software. The geo-location information in images and additional ground control points (GCPs) can be used for geometric correction (Rauste et al., 2007). In the case of the SNAP software, this was solved with the help of SRTM elevation model.

4.2.3. View angle correction of SAR images

Due to the imaging geometry, the Sentinel data is collected with different view angles. When this data is used for comparison, it is necessary to eliminate backscatter differences caused by this angular variability. The correction is usually done by normalizing the incidence angle with a reference angle (O'Grady et al., 2013). Equation 6 is used for normalizing.

$$\sigma^{\circ}{}_{ref} = \sigma^{\circ}\frac{\cos^n(\theta_{ref})}{\cos^n(\theta_v)} \qquad \text{Equation 6}$$

Where θ_v is the view angle [°]; $\sigma^{\circ}{}_{ref}$ is the backscatter normalized to the reference angle, θ_{ref} [m^2 m^{-2}], *n* depends on the type of scattering and the land cover characteristics which is usually between 1 and 2; the power *n* taken equal to 1 applies when volume scattering is dominant(Velde et al., 2014).

The view angle (θ_v) of each test sites was aggregated from SAR images by using SNAP. The average view angle of each test sites was calculated. The view angle is mainly varies about 34° and 43° , depending on the orbit from which the image was taken. The average view angle is 38.9° , so, this value was used as the reference angle (θ_{ref}).

4.2.4. Speckle filtering of SAR images

Speckle noise is very common in SAR images. The appearance of speckle makes the details and patterns unclear. Filtering techniques are applied to SAR images to facilitate interpretation. SNAP software was used to filter speckle in this study. The filter tool in SNAP includes Median, Lee, Refined Lee, Frost and Gamma-Map filters, from which an optimal one was selected through visual analyses. Figure 9 displays the test result of different filters on Sentinel-1 image acquired in 16th March, 2016. It can be seen that the Refined Lee filter gives the best result, the ponding water boundary becomes more clear.

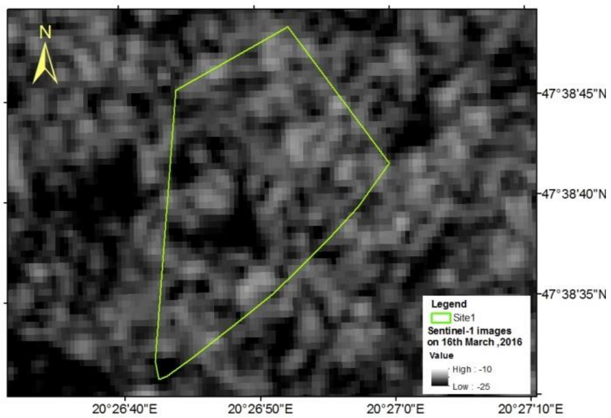

(a)Original Map unfiltered image

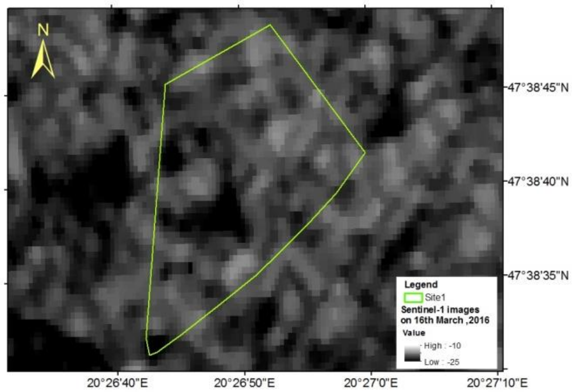

(b) Median filter

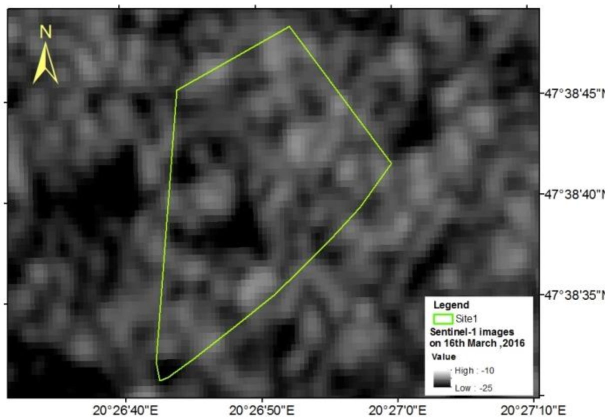

(c)Lee filter

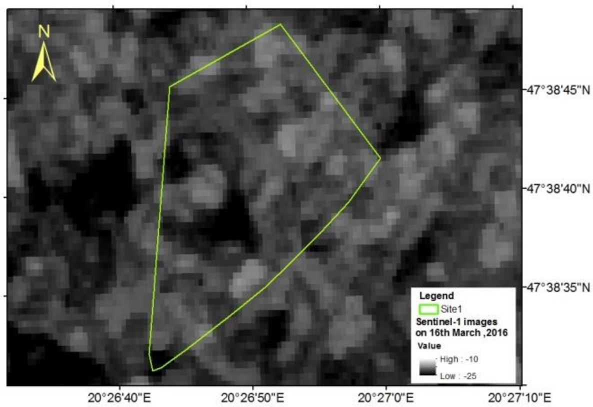

(d)Refined Lee filter

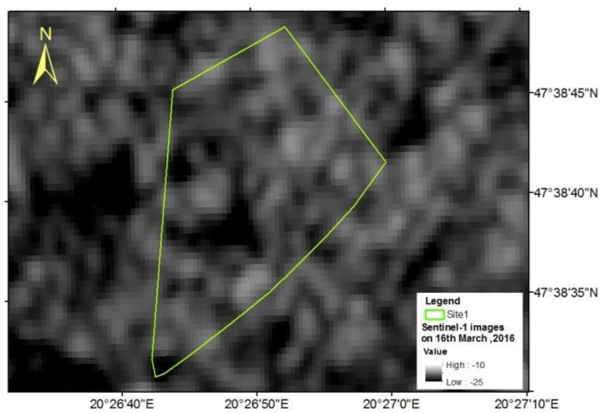

(e)Frost filter

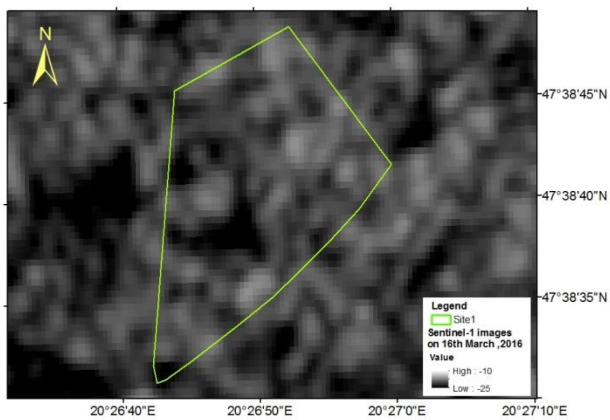

(f) Gamma-Map filter

Figure 8 SAR image with different filters

4.2.5. Atmospheric correction of VIS/NIR images

In order to retrieve the surface reflectance from VIS/NIR remote sensing images, the influence of atmosphere was corrected by Dark Object Subtraction (DOS) correction method. The downloading of Sentinel-2 (S-2) images and Landsat8 images was done from the Semi-Automatic Classification Plugin in QGIS. DOS atmosphere correction is an image-based atmospheric correction method. This method assumes that some objects must have zero reflectance, for example, water bodies or some area which is completely sheltered under shadow (Lantzanakis, Mitraka & Chrysoulakis, 2017). Actually, the scattering and absorption over the top of atmosphere makes the images have non-zero DN value over these dark objects. All of these non-zero values need to be defined in the images and subtracted from the whole band. For applying the atmosphere correction, DN value needs to be converted into TOA (top of atmosphere) Reflectance. TOA Reflectance computation needs the Equation 7.

$$\rho_k(i,j) = \frac{\pi * CN_{k,NTDI}(i,j)}{A_{k,NTDI} * E_S * d(t) * \cos(\theta_S(i,j))} \qquad \text{Equation 7}$$

$$\mathrm{d(t)} = \frac{1}{(1-0.01673*\cos(0.0172*(t-2)))^2} \qquad \text{Equation 8}$$

where: ρ_k is the TOA reflectance; $\mathrm{CN_{k,NTDI}}$ is the equalized numeric digital count of the pixel (i,j) with NTDI, NTDI is the number of S-2 TDI (Time Delayed Integration) lines; E_S is the equivalent extra-terrestrial solar spectrum and depends on the spectral response of the S-2 bands; the component $d(t)$ is the correction for the sun-Earth distance variation (see Equation 8); t is the Julian Day corresponding to the acquisition date (Julian day starts count since 01/01/1950) (ESA, 2016a).

4.2.6. Integration of Sentinel-2 images and Landsat 8.

In order to have NDVI value as much as possible, both Sentinel-2 (S-2) and Landsat 8 images are used in this research. But, S-2 and Landsat 8 has different wavelength range (Appendix 2). For S-2, the wavelength of band 4 (Red) is from 0.65 to 0.68 and the wavelength of band 8 (Near Infrared) is from 0.79 to 0.90. For Landsat 8, the wavelength of band 4 (Red) is from 0.64 to 0.67 and the wavelength of band 8 (Near Infrared) is from 0.85 to 0.88. So, the integration is necessary. Both S-2 and Landsat 8 satellite pass the study area on 20th May, 2016. The 2 NDVI maps on this day were used to compare, and get a conversion equation. The equations in Figure 9 can be used for converting NDVI value got from S-2 into NDVI value got from Landsat 8.

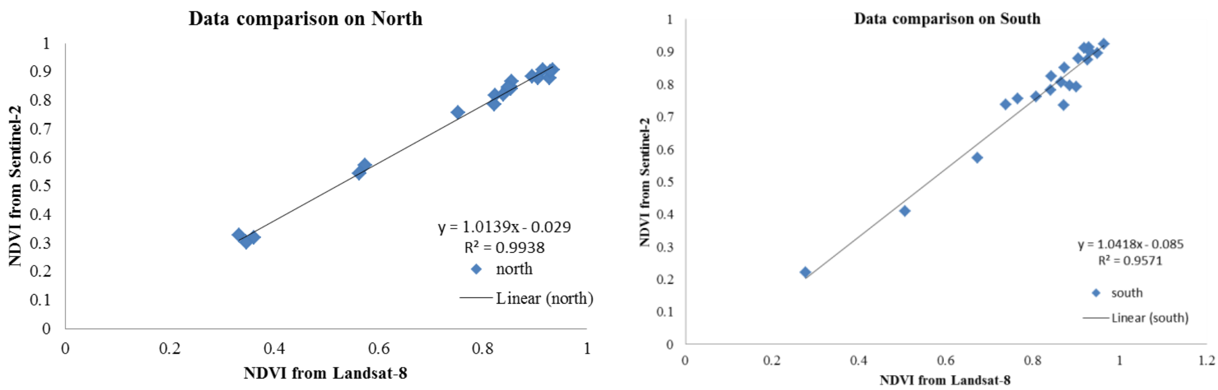

Figure 9 Comparison between Sentinel-2 data and Landsat 8 data

4.3. Time series analysis

Time series plots were made to see how backscatter coefficient, polarization ratio, NDVI, rainfall and soil moisture content changes through time. Agricultural fields have a high backscatter temporal variability because of the influence of vegetation growth, soil moisture changes and cultivation phenology (Bruzzone et al., 2004). So, the time series analysis was used to derive information about ground surface dynamic and crop growth stages (Moran et al., 2012).

4.3.1. Time series analysis of backscatter coefficient

The average backscatter coefficient of each test site was aggregated from SAR images. The SAR images from October, 2015 to October, 2016 were used for extracting backscatter coefficient using several masks. For each test site, some small masks were used for observing the detail based on the pixel level. Based on visual interpretation of the drone and radar images, some small masks were created to represent the area affected by the ponding water. The masks were set in the central part of the ponding water to avoid the influence of mixed pixels on the edges. There were also masks created for covering the non-inundation area. The mask polygons were manually digitized and then used for mean backscatter coefficient calculation for the various areas. The speckle effect reduced by calculation the real average. It is assumed that every mask covers homogenous areas. The standard deviation was used for quantifying the homogeneity of the masks (Equation 9). Time series can display the changes of the backscatter to identify ponding water and its inundation period.

$$stdev = \sqrt{\frac{1}{M} * \sum_{i=1}^{M} \sigma_i^2 - \sigma_{ave}^2} \qquad \text{Equation 9}$$

where, *stdev* is the standard deviation of the backscatter coefficient of a mask; *M* is the number of pixels in the mask; σ_i is the backscatter of the i^th^ pixel extracted from SAR images; σ_{ave} is the average of the backscatter coefficients of the mask

Rainfall and soil moisture time series were also used as ancillary data and compared with backscatter time series. The water bodies have smooth surface resulting in low backscatter observation in SAR images. The low value backscatter in SAR image could be coming from ponding water. But it can also be the result of low soil moisture content or smooth land surface without canopy. In our test area, rainfall is the main cause of ponding water The impeded infiltration of rainfall or excessive rainfall coming to the saturated soil can lead to ponding water. So, the rainfall and soil moisture data should be used to demonstrate the origin of the low backscatter.

4.3.2. Time series analysis of polarization ratio

σ^0_{vv} is sensitive to moisture and cross-polarized (σ^o_{vh}) is particularly sensitive for monitoring both crop and soil conditions (Moran et al., 2012). Polarization ratio $\frac{\sigma^\circ_{VH}}{\sigma^\circ_{VV}}$ can be calculated to monitor vegetation and crops apart from the influence from sensor calibration and changing target moisture conditions (Jiao et al., 2009 & Mtamba et al., 2015) . The polarization ratio was calculated from Sentinel-1 images. The average polarization ratio of each mask was calculated for each test site. Correlation analysis between polarization and NDVI was also made for showing the relation between the polarization ratio and NDVI.

4.3.3. Time series analysis of NDVI

NDVI (Normalised Difference Vegetation Index) can be used as an indicator to reflect the coverage of vegetation, vegetation growth state and crop phenology (La, Del, & Hamsom, 1987). Its values are represented as a ratio ranging in value from -1 to 1. Visible and Near-Infra-Red (NIR) bands from atmospheric corrected images can be used for NDVI calculation (Rouse, J. W. et al., 1973)(Equation 10).

$$NDVI = \frac{NIR-VIS}{NIR+VIS} \qquad \text{Equation 10}$$

where NDVI is Normalised Difference Vegetation Index; VIS is the reflectance in the red visible band; NIR is the reflectance in Near-Infra-Red band.

The temporal patterns of NDVI are used for land cover change detection and large area crop mapping (Lenney et al., 1996 & Wardlow et al., 2007 & Wardlow & Egbert, 2008). Due to the crop phenology, the value of NDVI changes (Wardlow & Egbert, 2008). Fields covered by crops have a high NDVI value at the peak plant growth period and have a low NDVI value at ploughing and harvest (Lenney et al., 1996). Ponding water can damage the crop in the field which results in the decrease of the NDVI value. Thus, multi-temporal NDVI maps can be used to identify the effect of inundation in agricultural areas based on the identifiable temporal pattern of the crops. The masks used to obtain the average backscatter coefficient are also used to calculate the NDVIs. The NDVI time series and backscatter coefficient time series are compared to locate the ponding water.

4.4. Ponding water mapping

In SAR images, ponding water usually produces a low backscatter coefficient response and appears dark. According to this feature, a low backscatter threshold can be extracted from the time series of backscatter coefficient. The pixel with a value less than the threshold is classified as ponding water. Inversely, the pixel with a value larger than the threshold is classified as non-inundated area. All the SAR images were classified by this method and to get a bit image. The area covered by water bodies got the value of 1. No-inundated areas have the value of 0. In order to distinguish the permanent water bodies (such as rivers and artificial ponds) and temporarily ponding water clearly, all the bit images were added up in ArcGIS by using raster calculation. The areas with the value same to number of calculated images was classified to be permanent water bodies. Otherwise, it belongs to temporarily ponding water. Then, ponding water spatial distribution map was mapped after overlaying the reclassified map with a Sentinel-2 map. In order to see the inundation duration of ponding water, a temporal distribution map was also made. Different values were given to the inundation map of different months. The applied values are shown in Table 2. Then, raster calculation was also used to add up all images. The new value in the result map can show the occurrence time of ponding water.

Table 2 The value used for ponding water temporal distribution mapping

Input value	**Month**	**January**	**February**	**March**	**April**
	Value	1001	1002	1003	10004
Result value	**Month**	**January, February**	**January, March**	**February, March**	**January, February, March**
	Value	2003	2004	2005	3006
	Month	**January, April**	**February, April**	**March, April**	**January, February, April**
	Value	11005	11006	11007	12007
	January, March, April	**February, March, April**	**January, February, March, April**		
	12008	12009	13010		

5. RESULTS AND DISCUSSION

5.1. Backscatter analysis and ponding water identification

Frulla et al. (1998) stated that: "although σ° can be calculated for every pixel, it has a physical meaning when it is averaged over a group of pixels corresponding to a distributed target in the image". So, in this study, the average backscatter coefficient was calculated by several polygon masks which cover homogeneous pixels. The average calculation can also benefit in reducing the speckle effect. VV polarized backscatter was selected to detect the ponding water because VV backscatter time series is more sensitive to soil moisture which can show more detail about water surface. All of the SAR images used in this research were collected from the ascending orbit. But part of images have an average incidence angle of 34° and others have an average incidence angle of 43° .All the images have the incidence angle around 34° belongs to Ascending 1 group. The images have 43° belongs to Ascending 2 group. The difference of incidence angle results in the differences in backscatter coefficient (Gauthier, Bernier, & Fortin, 1998). Although the angle correction was done for all images using Equation 6, differences in backscatter still existed between the two groups. This was most probably due to the selected *n* value, which is highly dependent on the physical properties of the surface. We tried to optimize it with least square fitting, but more accurate data would have been needed about the canopy properties (height, roughness), going well beyond the objectives of this thesis, so a simpler solution was looked for. In order to observe the trend of backscatter without the influence of incidence angle, 2 sets of images with a different incidence angle are separated to make plots.

The mask polygon selection was based on drone image and SAR images. Figure 11 shows the drone image used for mask selection. In the northern area, Mask site1 covers the whole field. Mask site 1a covers the core of the area affected by ponding water. Mask site 1b covers a bit wider area affected by ponding water. These affected areas appear white in the drone images and were cross-checked by visual interpretation of the SAR time series too. Mask site 1c covers an area without the influence of ponding water. Where drone images were not available, the mask polygon selection was based on a series of SAR images. One or two masks were used to cover the dark area with low backscatter values, i.e., the inundated areas. Another mask was used to cover the brighter, non-inundated areas.

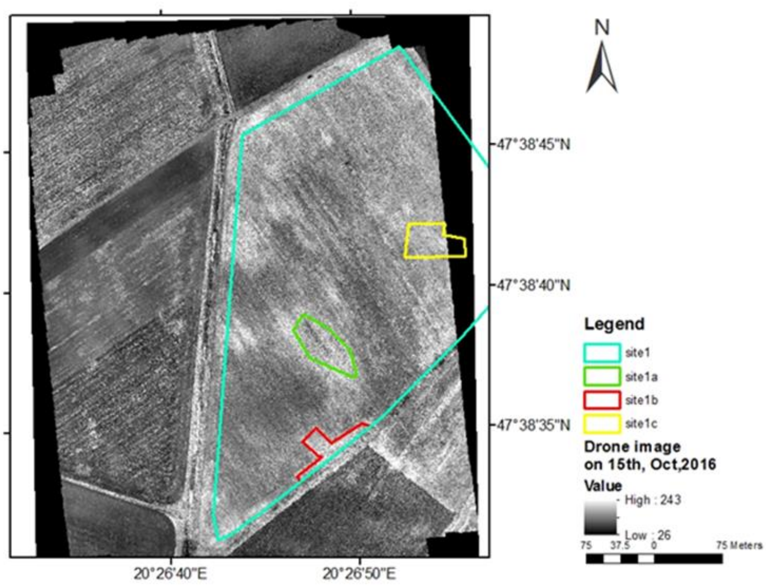

Figure 10 Drone image and mask polygon selection over northern test site1

5.1.1. Northern study area

Figure 12 shows the time series of backscatter over the northern test site 1. There is an obvious decrease in the backscatter of site 1a (Figure 12, a) from the original value around -8dB to about -18 dB around January. Then, the backscatter value stays at about -18 dB until 1st, March. There is also a short low value period on the backscatter time series of site 1b (Figure 12, b). The backscatter decreases to -17.6 dB around January and just stays at low value for 1 month. Water bodies usually produce a low backscatter coefficient response. So, the decrease of the backscatter can be related to ponding water. Inversely, time series of Site 1c (Figure 12, c) has the backscatter value larger than -16 dB and the backscatter increases slightly from -16 dB to -12 dB within these 3 months. This area was not flooded in this period. The increase is most probably due to the increased soil moisture as a result of rainfall and the melt of snow cover. From the daily precipitation data, it can be seen that there was intensive rainfall from January to March. The rainfall makes the soil wet which can increases the backscatter. Also, there was snow in the field in January. The snow cover can moisten the soil after it has melted. Comparing the three time series in Figure 12, the intensive rainfall increases the backscatter over non-inundated area but decrease the backscatter over site 1a and 1b. So, it can be concluded that there was ponding water in the field. The ponding water over site 1a remained for 3 months from January to March. But for site 1b, the ponding water was quite shallow and just stayed in the field during January.

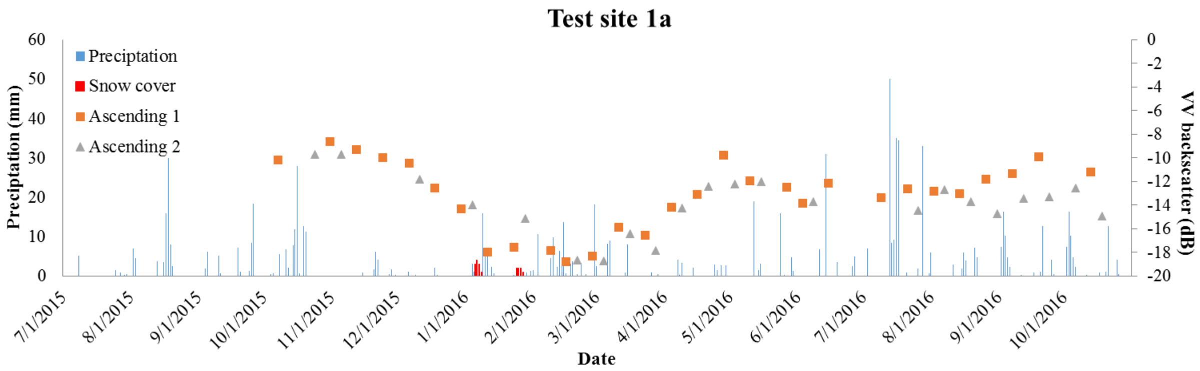

(a)

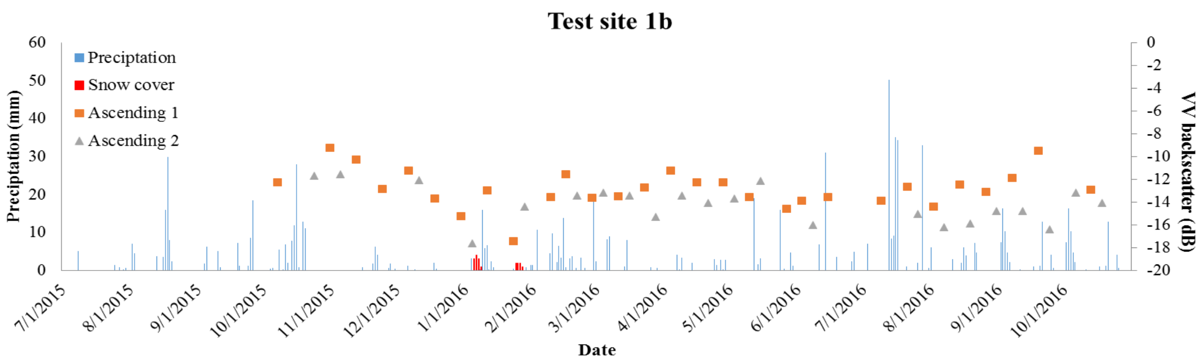

(b)

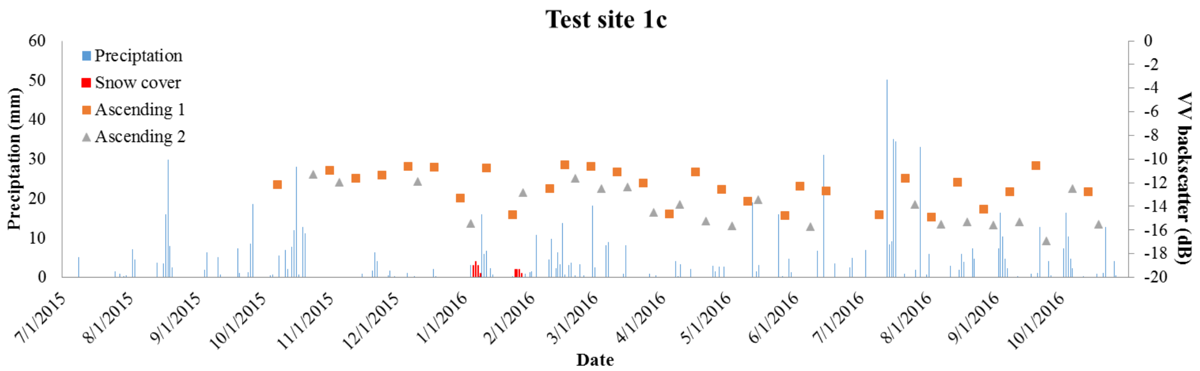

(c)

Figure 11 Backscatter time series of northern site 1

Figure 13 shows the backscatter time series over the northern site 2. The low backscatter period is also very obvious shown on the time series of site 2a and 2b (Figure 13, a, b). The backscatter decreases to around -19.3 dB and stays at this low value from the end of January to the start of April. There was limited rainfall in December which makes the soil very dry. So, the backscatter starts to decrease since the end of December. Then, there was an intensive rainfall and snow around the on the beginning of January. The rainfall and the snowmelt moisten the soil and make the soil became saturated. It leads the backscatter jumps back to-13.5 dB on 23rd, Jan. After that, the water accumulated in the field which leads the backscatter stays at around -18.5 dB until the end of March. The increase of backscatter over site 2c (non-inundated area) and the daily rainfall data can also show that the ponding water affects site 2 from January to March. From the end of April to the start of May, site 2a and 2b (about -13 dB) has a higher backscatter than site 2c (about -18 dB). Because the soil in site 2a and 2b stores more moisture after inundation and becomes more easily wet than the non-inundated areas once precipitation happens. The wet soil has a larger dielectric constant than the same surface with lower moisture content, which results in higher backscattering. There was not much precipitation in this period. For site 2c, the soil was very dry which results in low backscatter.

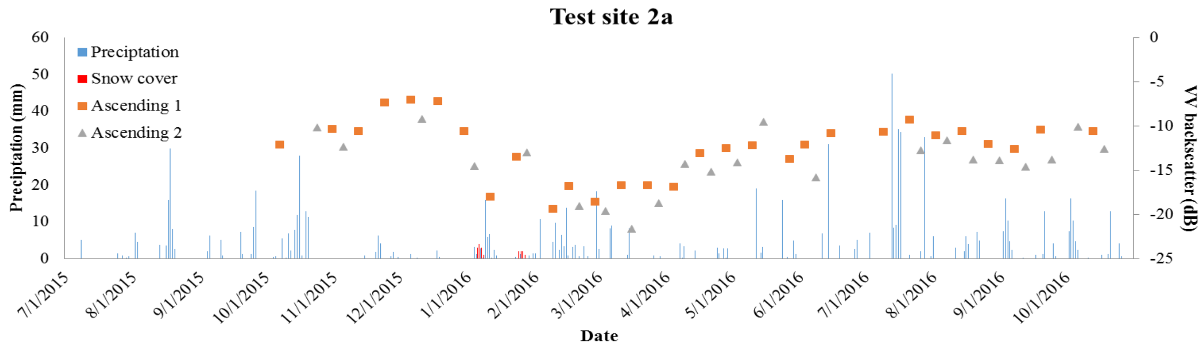

(a)

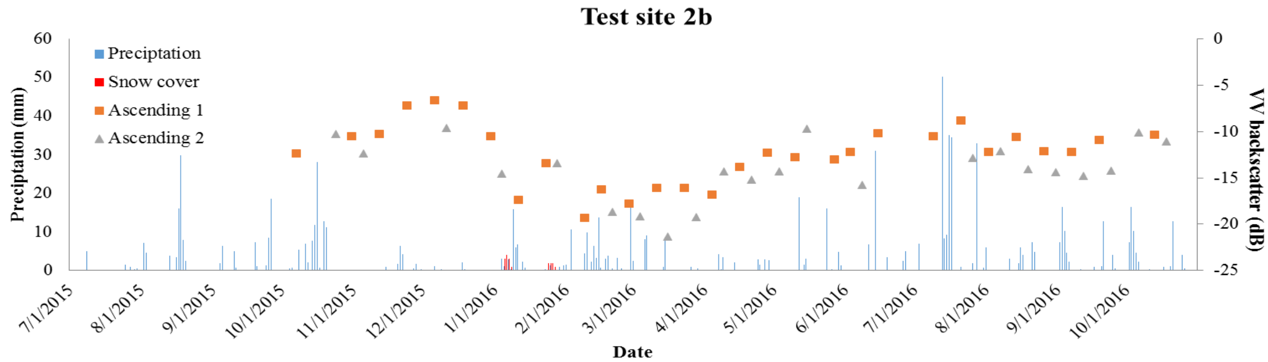

(b)

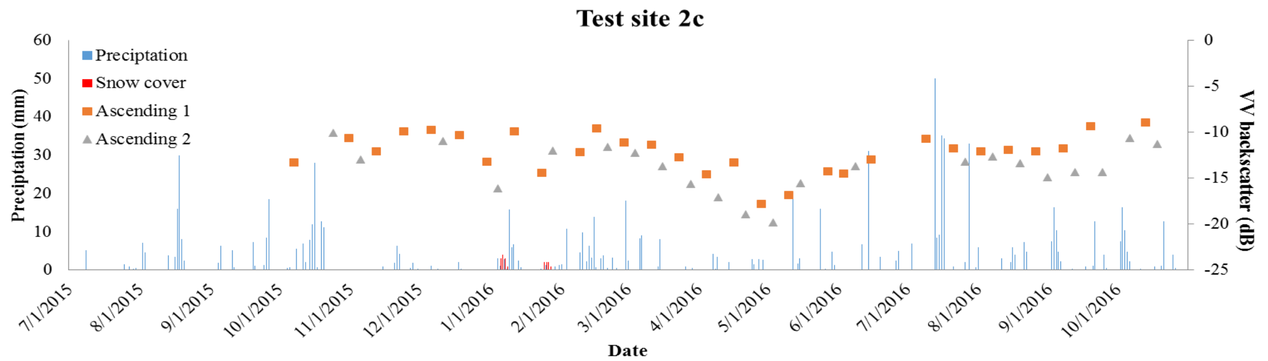

(c)

Figure 12 Backscatter time series of north site 2

The 3 plots in Figure 14 display the backscatter time series over site 3. The time series of site 3a and 3b shows 3 times decreasing on backscatter. The first decreasing happened from February to March which makes the backscatter decreases to -14.38 dB. The other 2 decreasing happened on May (-14.36 dB) and September (-15.82 dB) when the rainfall was not much. Compared with the backscatter time series of site 3c, it can be seen that the backscatter increases over the non-inundated area from February to March but also decreases on May and September. Because of the intensive precipitation happened in February and March, it can be argued that ponding water was in this field during February and March. But for non-inundation area, the soil gets saturated easily and then water accumulates in the field which leads to the decreasing of backscatter. The rainfall moistened the soil which increases the backscatter of non-inundation area. For the decreasing in May and September, it results from the dry soil because of the insufficient precipitation.

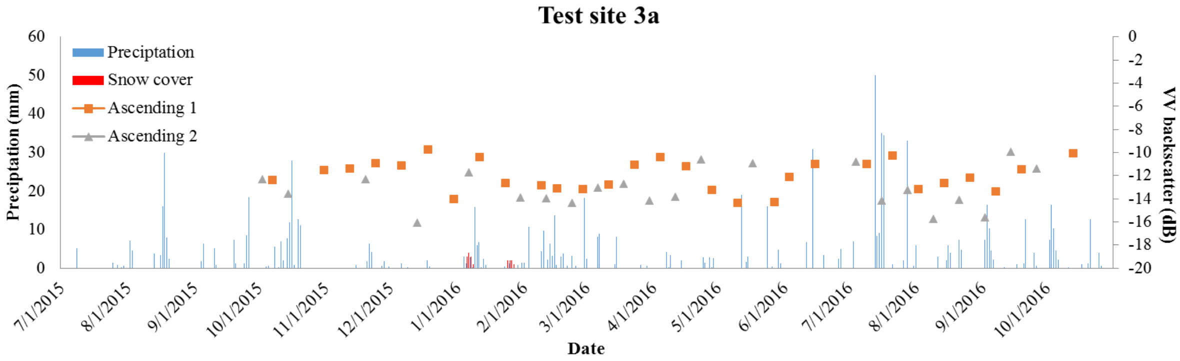

(a)

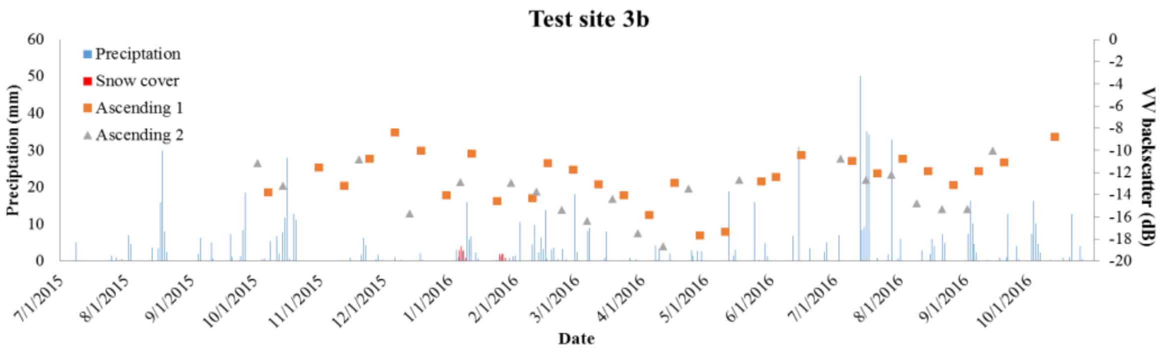

(b)

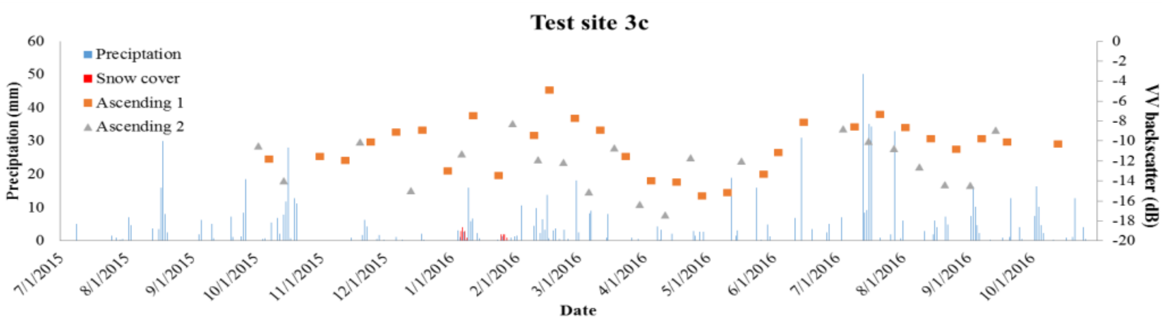

(c)

Figure 13 Backscatter time series of northern site 3

Ponding water cannot be identified over a long period. As it shown in Figure 15, the backscatter coefficient over test site 4 fluctuates at a value between -6 dB and -14 dB. Three plots share the same increasing and decreasing pattern which also has a good agreement with the daily precipitation time series. The backscatter decreases in November and December when the rainfall is very limited. The snow and rain in the beginning of January causes the saturation of the soil (high backscatter after the rainy period on 11th, January), then the backscatter drops sharply, due to a short surface water ponding. Then, the backscatter increases from the 16th February to March and then in July when the rainfall is sufficient.

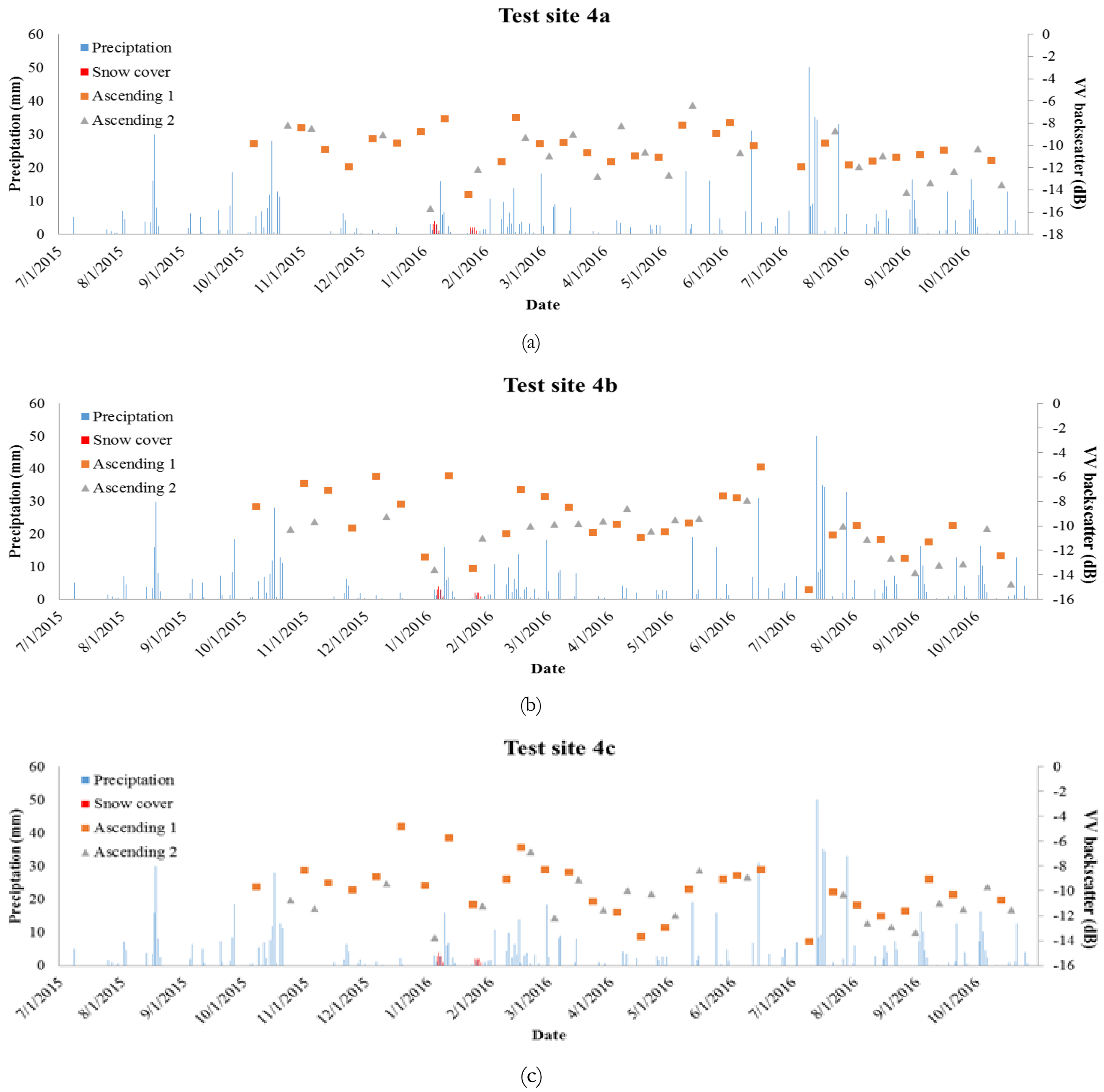

Figure 14 Backscatter time series of northern site 4

The soil moisture over site 5a and 5b is compared with the backscatter time series in Figure 16. The soil moisture of the top 15 cm was measured only from the end of April to the end of July. The soil moisture time series follows the pattern of the backscatter time series. The soil moisture was measured at 15 cm depth underground but the backscatter can only reflect the change on surface. So, soil moisture has some delay response to the backscatter time series. There is no obvious long term ponding water to be identified from the time series. The backscatter just increases when there is plenty rainfall and decreases when there is not sufficient rainfall.

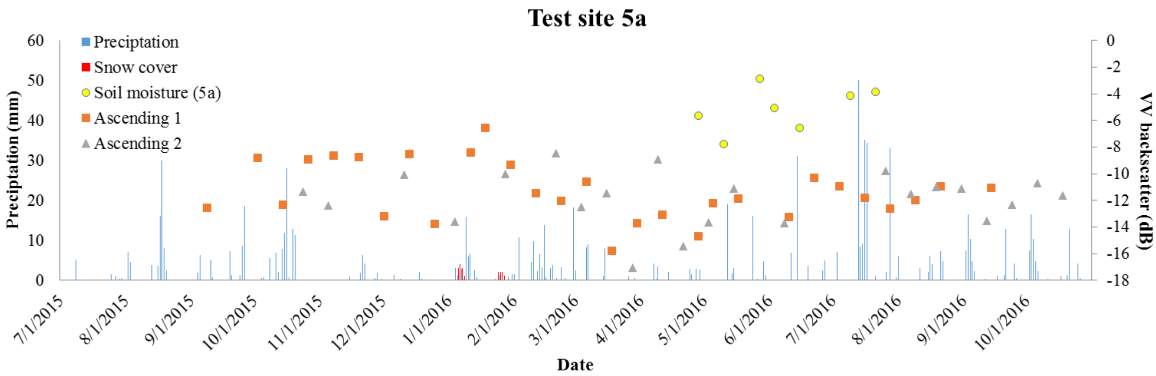

(a)

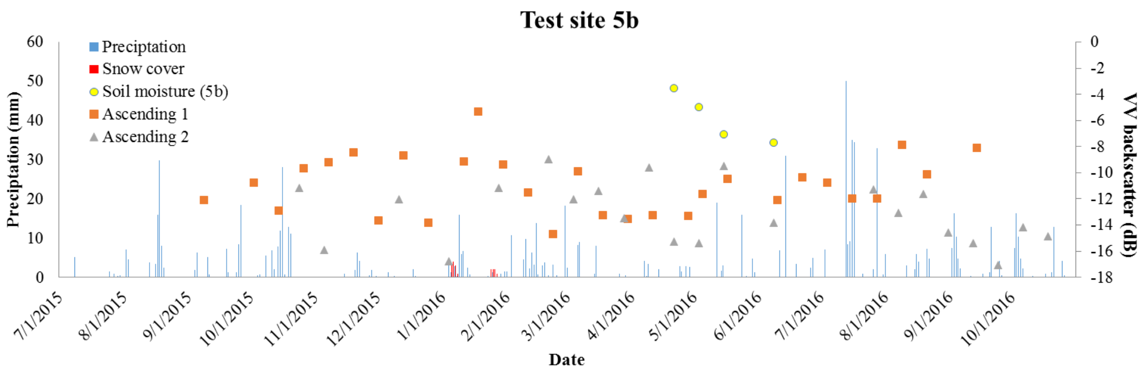

(b)

Figure 15 Backscatter time series of northern site 4

During the field work, in-situ soil moisture was measured over site 1, site 3 and site5. Soil moisture measurement was carried out over the inundated areas and the non-inundated area which were identified by the local farmers. The measurement locations were coinciding with the masks used in this study. The measurement result shows in Table 3. It can be found that the area which is prone to ponding water usually has higher soil moisture content. For site1, site 1a has more wet soil than site 1c. When surplus rainfall comes to the ground, the soil over site 1a is more easily get saturated than site 1c. For site3, measured was carried out at a low place which is near site3a and a high place which is near site 3c. The high place usually cannot store water, so ponding excess water never happens here. But the low place makes it easier to accumulate water. So, the soil moisture is higher in the low place than high place. For site 5, the site 5b has lower soil moisture which is less prone to the ponding water.

Table 3 In-situ soil moisture data measured during the field work

Site	Soil Moisture(m^3/m^3)	Remarks
Site1	0.137	47°38'38.42"N,20°26'45.86" Ponding water often occur, very near to site1a
	0.115	47°38'45.07"N, 20°26'51.11"E No ponding water near very near to site1c
Site 3	0.224	47°42'50.43"N,20°25'52.19"E Ponding water exist, low place, site3a
	0.117	47°42'48.61"N, 20°25'41.57"E High place, site3c
Site 5	0.138	47°40'2.5 "N, 20°25'7.04"E Non-inundation area, Near site5b
	0.166	47°40'2.14"N, 20°25'6.08"E Inundation area

Comparing all the time series plots over the northern study area, it can be found that test sites 1, 2 and 3 were affected by ponding water seriously during January to March. All the time series of these 3 test sites have obvious low backscatter periods in response to the increase of precipitation. The backscatter in this period decreases to less than -14 dB. The rainfall can make the soil moisture increase and then result in the increasing of VV backscatter. But when the soil is saturated, the water just starts to accumulate on the surface and form ponding water which result in the decreasing of backscatter. From the crop information got from the local farmer, the main soil content is clay in the northern study area. The proportion of clay is 42~44% (Appendix 1). The infiltration rate of clay is 1-5 mm/hour (C. Brouwer, 1988). This kind of heavy soil has a very low infiltration rate which leads the ponding water happens easily.

5.1.2. South study area

For the southern study area, more soil moisture data was collected to find the relation between rainfall, soil moisture and VV backscatter and use them to identify the ponding water in the field. As it is shown in Figure 17 (c), the VV backscatter responses rainfall and soil moisture with the similar changing patterns over non-inundated area (southern site 1c). The rainfall is abundant in February, March, June and July. The soil moisture and VV backscatter also has significant increasing during these months. But for southern site 1a and 1b, the VV backscatter decreases to -17 ~ -19dB while the rainfall and soil moisture increases from February to March (Figure 17, a, b). The rainfall increases the soil moisture over site 1a and 1b. The low backscatter results from the increasing rainfall and soil moisture. So, the low backscatter period can be considered as the result of ponding water.

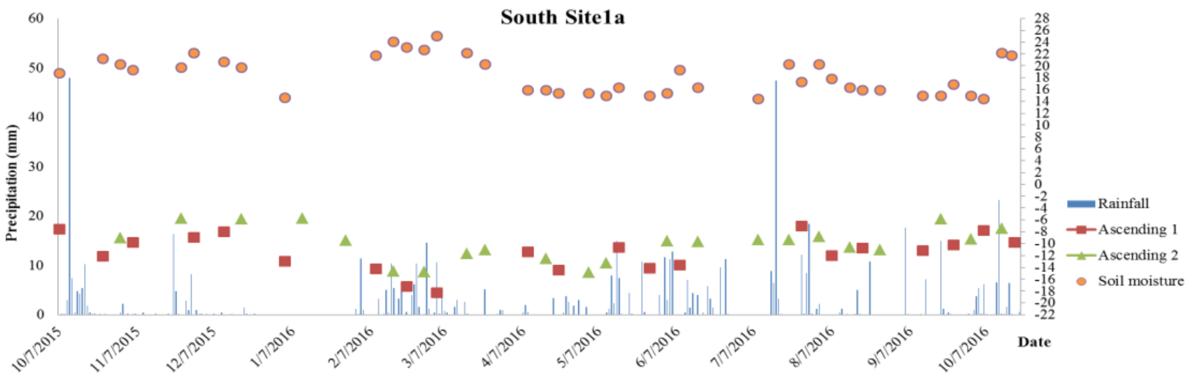

(a)

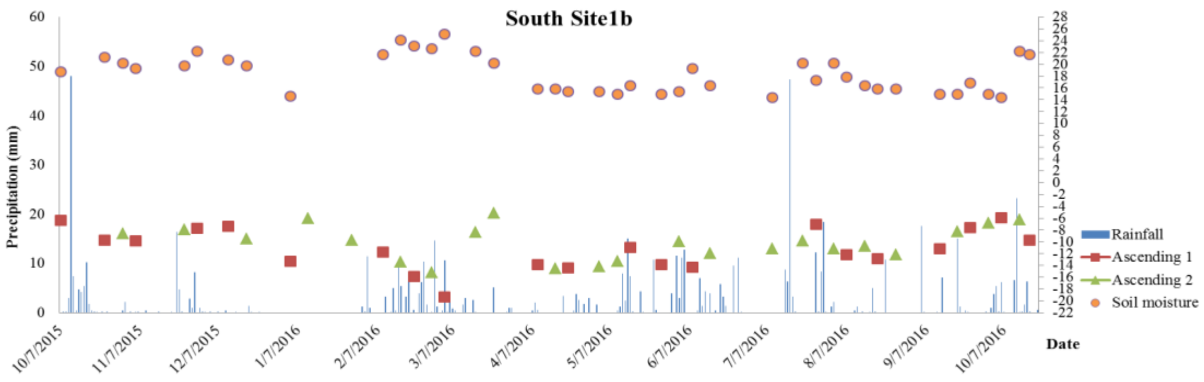

(b)

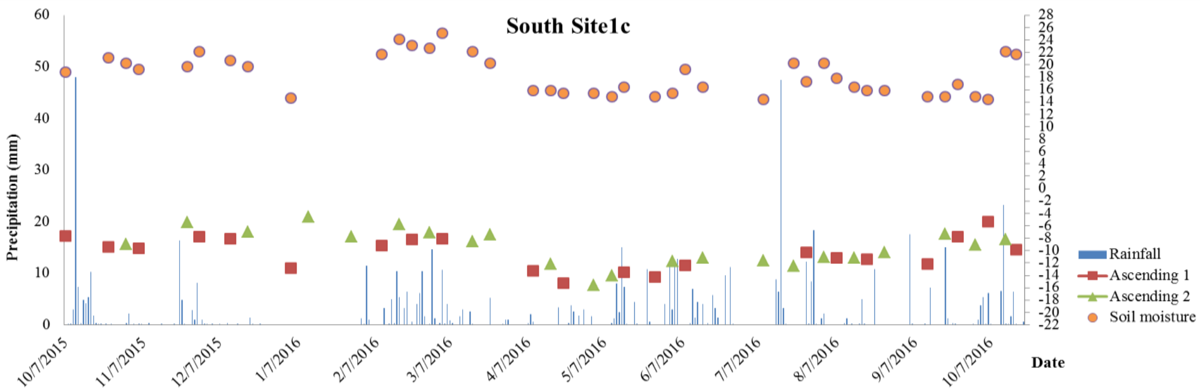

(c)

Figure 16 Backscatter time series of southern site1

It can also be found that the ponding water affected southern site 2 from February to March. From Figure 18, it can be seen that the backscatter of southern site 2a decreases to -18.77 dB during March. The soil moisture increases from 22% to 25% during the same time period. However, in the time series of non-inundated (southern site 2b), the backscatter increases from -11 dB to -6 dB during March. So, the low backscatter period in the backscatter time series of site2a results from the rainfall. The rainfall moistens the soil first and then leads the ponding water form over the saturated soil. The smooth ponding water surface makes the backscatter decrease.

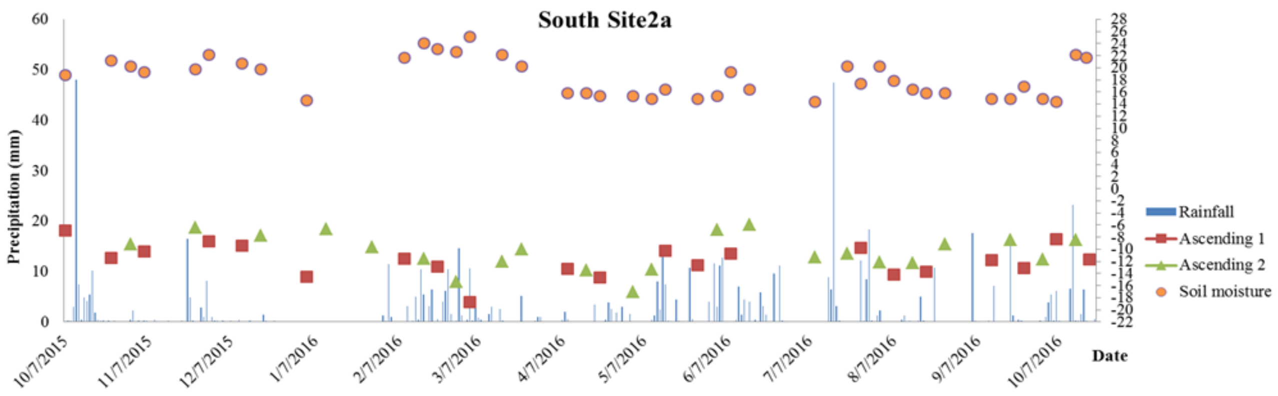

(a)

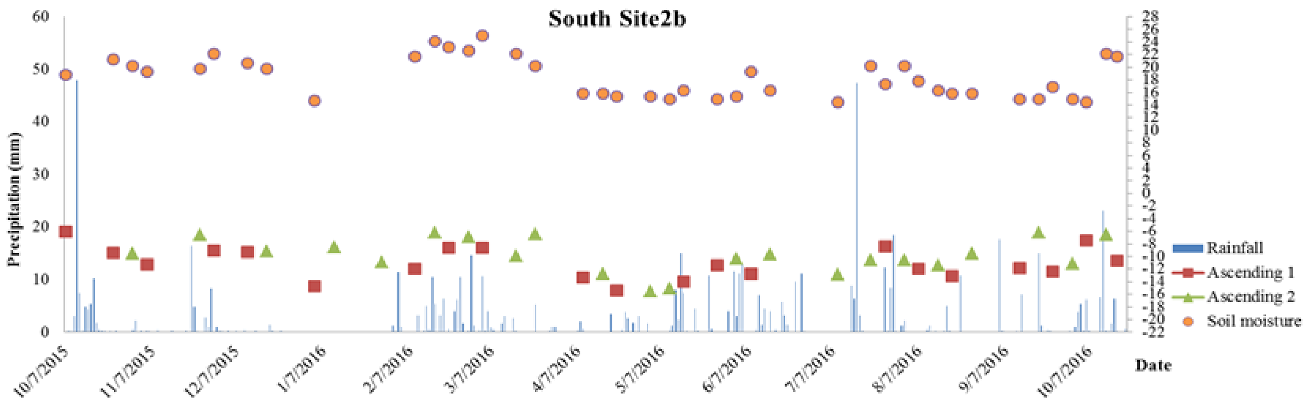

(b)

Figure 17 Backscatter time series of southern site2

Figure 19 shows the time series over southern site 3 and 4. The soil moisture is in a good agreement with the rainfall. The backscatter time series of site 3 fluctuates from -5 dB to -15dB. The backscatter time series of site 4 fluctuates from -8 dB to -19dB. There is no low backscatter in the time series of site3. For site 4, the backscatter decrease to around -17 dB or even -19 dB at the end of April. But from the soil moisture time series, the low backscatter results from the dry soil. So, ponding water did not come to site 3 and 4 during the period under investigation.

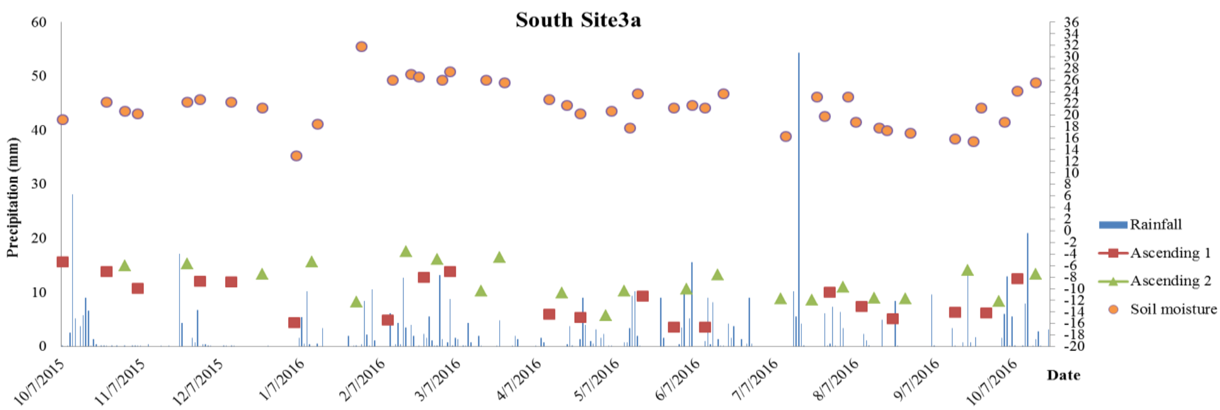

(a)

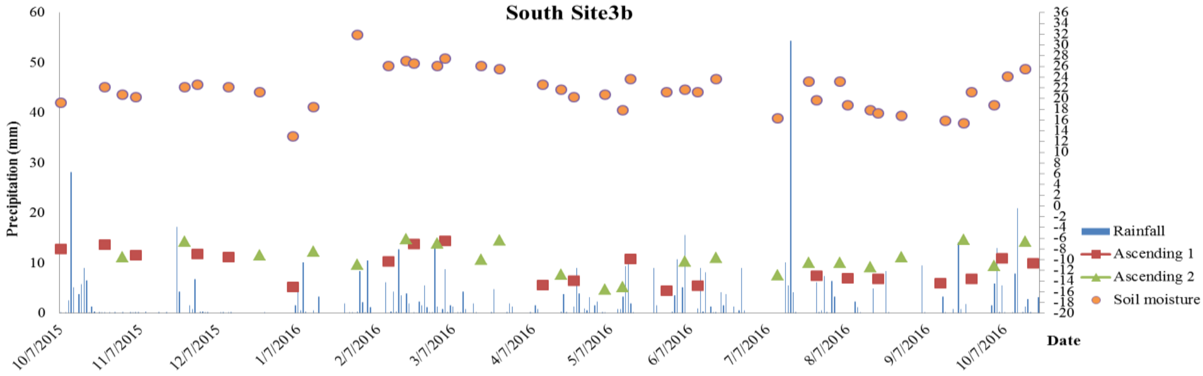

(b)

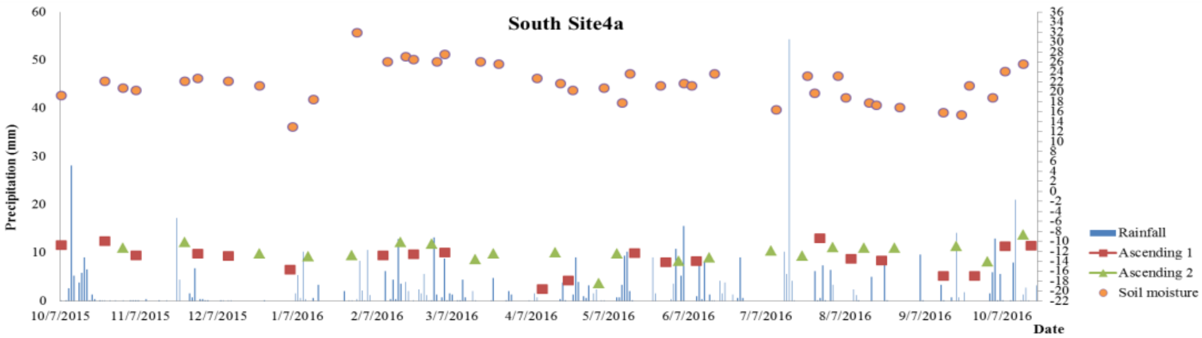

(c)

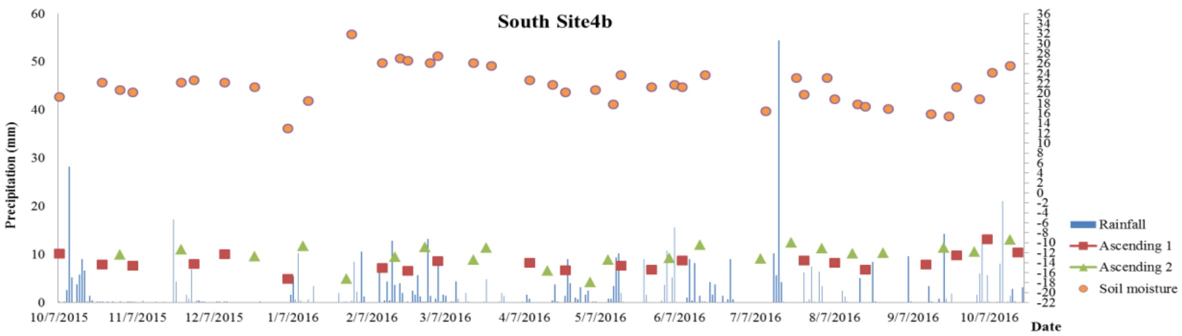

(d)

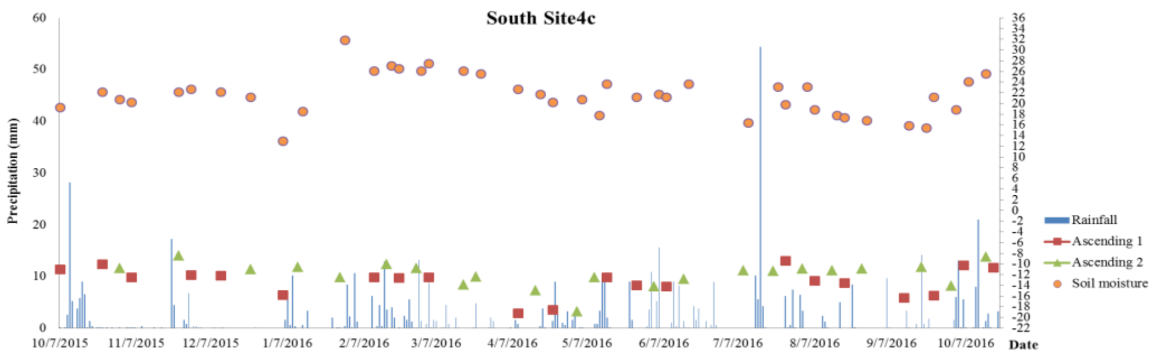

(e)

Figure 18 Backscatter time series of southern site3 and 4

Fortunately, the done image captured little ponding water on test site 4. The drone image was taken on 27th, October, 2016 by team of the University of Szeged, under the coordination of Dr. Bouderwin van Leeuwen. The drone image is shown in Figure 20 (a). Ponding water can be seen in the image where the red circle area is zoomed in. Sentinel-1A did not pass by this field on 27th, October but a Sentinel-1B image acquired on 28th, October is available. This SAR image is shown in Figure 20 (b). Compared with the drone image, the SAR image has low backscatter area at the same place which indicates that the low backscatter represents the ponding water.

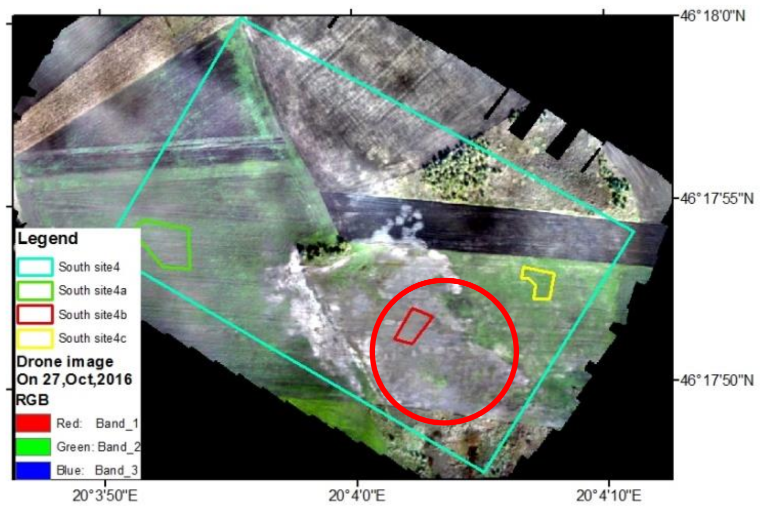

(a)

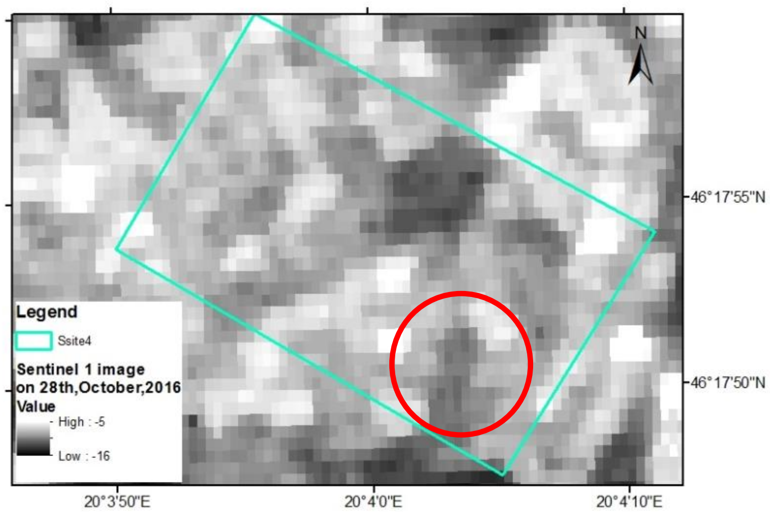

(b)

Figure 19 Comparison between drone image (a) and SAR image (b)

Comparing all the time series plots of southern study area, it can be seen that the rainfall leads to the increase of soil moisture. Soil moisture also has a good agreement in backscatter over non-inundated areas. Regression lines were calculated made between VV backscatter and soil moisture to analyse the relation between them. Only the VV backscatter and soil moisture data of non-inundated area is used for the analysis. The result shows in Figure 21. The R^2 shows that the VV backscatter is well correlated with soil moisture. So, soil moisture is the dominant factor for the change of the VV backscatter. Thus, those low backscatter areas with high soil moisture content and high rainfall value must be affected by the ponding water.

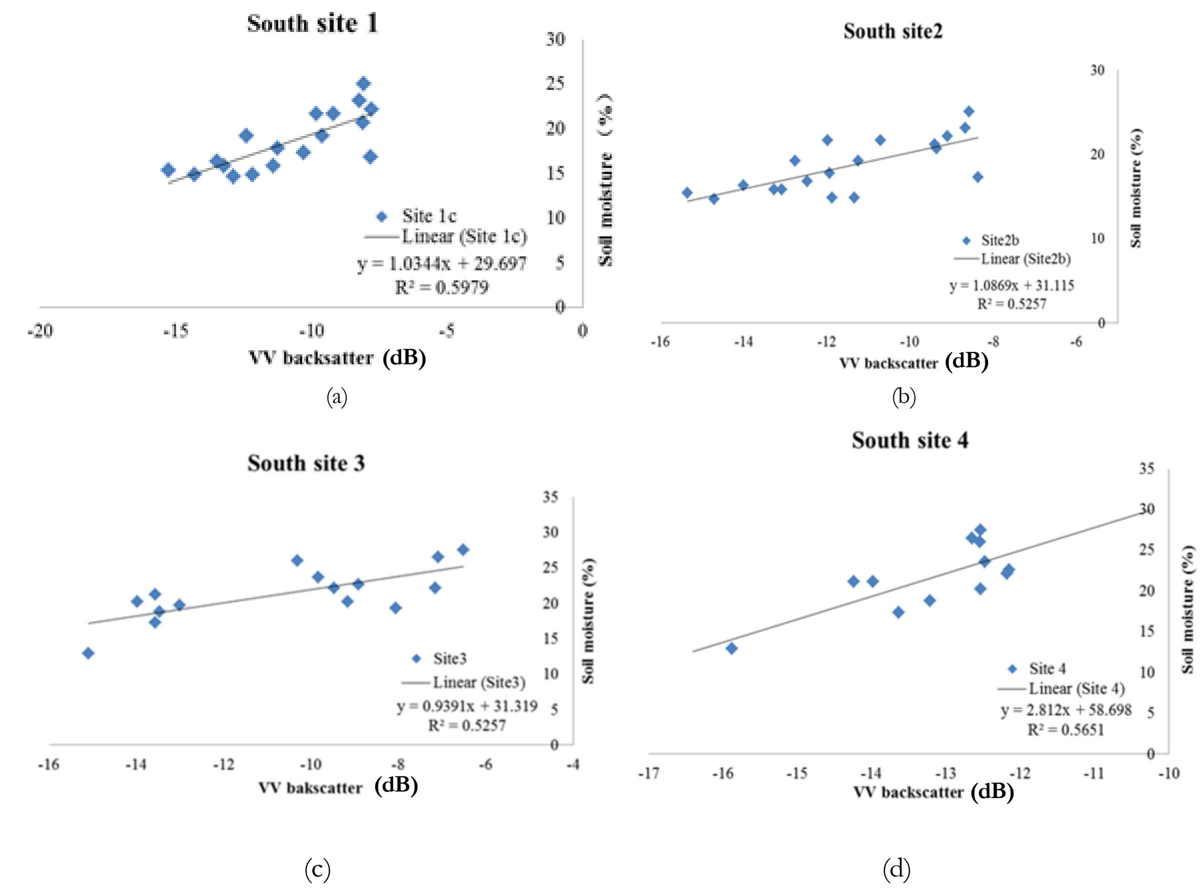

Figure 20 Relationship between VV backscatter and soil moisture

5.1.3. Incidence angle normalization

The difference between the backscatters from Ascending 1 images and 2 images can be found from the time series. The average of the two adjacent values in the Ascending 1 group was calculated and compares the values with the corresponding dates in the Ascending 2 group. The differences were calculated and plotted in Figure 22. For site 5a, the backscatter difference is just around 1 dB before March. Then, the difference rises to around 3 dB from April to July. From August to September, the difference can be 5 dB. For site 5b, the backscatter difference is very little before April. Later, the difference can be 4-5 dB from August to September. From the crop information (Appendix 1), site 5 was ploughing before April. The canopy started to grow since April. So, the NDVI time series were compared with the backscatter difference in Figure 22. It can be found that the trend of differences match the NDVI pattern. The R^2 got from the correlation analysis shows the limited relation between NDVI and backscatter differences. The R^2 of site 5a is 0.47 and the R^2 of site 5b is 0.53. So, the backscatter differences between two kinds of ascending images depend on the land cover.

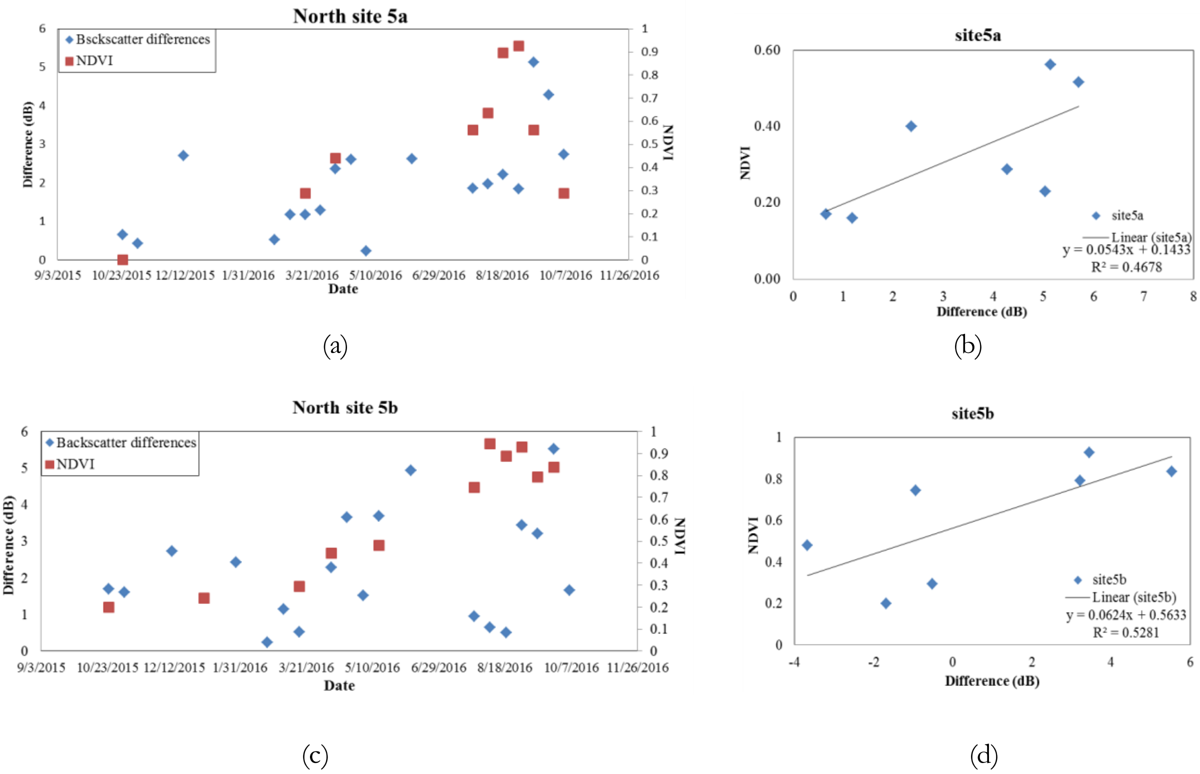

Figure 21 Relation between the backscatter different and NDVI

In order to use the ascending 1 and 2 images together, the incidence angle correction was applied in the pre-processing step. A reference angle which is 38.9° was used to normalize the backscatter. But the differences still exist because the angle correction was done based on an assumption. That the land cover does not change through the time. When the Equation 6 was applied for angle correction, the *n* used in the equation was applied to 1. But the fact is that the land cover of the field changed through the study period and different *n* value should be applied in the angle correction equation for different phonological stages of the crops.

Northern site 1 was used to analyse and find the optimal *n* for different canopy properties (Table 4). Water bodies, bare land and alfalfa were considered as the possible land cover. Bare land 1 is the area usually affected by ponding water during the inundation period. Bare land 2 is the area which is never affected by ponding water. The optimal *n* was found by minimizing the backscatter difference between Ascending 1 and 2 images. From the result in Table 4, it can be seen that different optimal *n* was calculated for different land cover types. For 2 different kind bare lands, the optimal *n* is quite close to each other. The area covered by the alfalfa need the lowest *n* which is below 0. For bare land, the n should be 3.96.

Table 4 Optimal *n* based on land cover

	Ascending 1				Ascending 2							
	Date	**Intensity (m^2 m^{-2})**	**Incidence angel (°)**	**Backscatter (dB)**	**Date**	**Intensity (m^2 m^{-2})**	**Incidence angel (°)**	**Backscatter (dB)**	**Differences**	**n**	**Average**	
Water	1/23/2016	0.019	34.8	-16.213	1/28/2016	0.033	43.78	-16.213	6.53E-08	-4.29	0.34	
	2/16/2016	0.012276	34.76	-19.151	2/21/2016	0.012	43.739	-19.151	9.88E-10	0.18		
	2/28/2016	0.01544	34.78	-18.427	3/4/2016	0.013	43.75	-18.427	2.60E-10	1.34		
	3/11/2016	0.029	34.76	-16.348	3/16/2016	0.017	43.78	-16.348	3.45E-08	4.13		
Bare land1	10/31/2015	0.167	34.79	-8.701	10/24/2015	0.1	43.8	-8.701	2.94E-09	3.97	3.77	3.96
	11/12/2015	0.148	34.75	-10.207	11/5/2015	0.052	43.77	-10.207	3.38E-08	8.10		
	12/18/2015	0.069	34.78	-11.436	12/11/2015	0.076	43.77	-11.436	4.42E-08	-0.75		
Bare land2	10/31/2015	0.079	34.235	-11.424	10/24/2015	0.065	43.321	-11.424	9.18E-11	1.53	4.14	
	11/12/2015	0.092	34.282	-12.078	11/5/2015	0.04	43.26	-12.078	1.08E-08	6.60		
	12/18/2015	0.069	34.78	-12.619	12/11/2015	0.041	43.3	-12.619	5.39E-11	4.30		
Alfalfa	4/4/2016	0.067	34.23	-11.649	4/9/2016	0.07	43.27	-11.649	5.70E-08	-0.34	-1.04	
	4/16/2016	0.053	34.22	-13.611	4/21/2016	0.035	43.32	-13.611	1.00E-08	3.24		
	4/28/2016	0.021	34.26	-15.203	5/3/2016	0.045	43.254	-15.203	5.60E-08	-6.03		

5.2. NDVI time series and crop growth monitoring

5.2.1. NDVI and crop height

NDVI time series were made for monitoring the crop growing condition. Figure 23 shows the NDVI change for all 5 test sites over northern study area.

Figure 23 (a) shows the NDVI over test site1. This field was covered by alfalfa. It can be seen from the plot, that the NDVI value increases from January (around 0.3) to May (0.5-0.6) and then had a quick decrease on June (0.4). Later, the NDVI value increases again from July to August (0.6-0.7) and decreases again on September (around 0.4). The trend of NDVI fits agricultural activity and crop height collected from local farmer (Appendix 1). According to the agricultural activity information, the alfalfa was growing from Oct, 2015 to May, 2016. The height of canopy grew from 10 cm to 50 cm. The first harvest was on June and it results in a decrease of NDVI. Later, the alfalfa grew again resulting in a second harvest in September. The NDVI value of site 1 starts to decrease from January onward and reaches its lowest value on 21st, March at 0.18. Site 1c (the non-inundated area) has a higher NDVI value during the same period and reaches 0.64 on 21st, March. Compared with the backscatter time series, the decrease of the NDVI can also prove ponding water existed in the field. Because the water bodies usually have low reflectance. When the inundation happens, it covers part of crops in the field and decreases the NDVI value on the multi-spectral images.

The same result can also be found on site 2. In Figure 23 (b), the NDVI of non-inundated area (site 2c) increases from 0.34 to 0.88 since January to May. But for site 2a, NDVI decreases close to 0 on the end of January and it only reaches 0.78 on May before harvest.

The NDVI time series over site 3 and 4 cannot show the influence of ponding water clearly. There is only a slight decrease of NDVI on March over site3c. From Figure 23 (c), the NDVI value increases gradually from Oct, 2015 to Jun, 2016, from around 0.2 to around 0.8. The height of wheat grew from 10 cm to 65-70 cm. After that the NDVI decreases on July because of harvest. Then, the rapeseed was sowed on August. The height of rapeseed grew from 5 cm to 20 cm, which reflects NDVI value of 0.2-0.3. It can be seen from Figure 23 (d), the NDVI increases gradually from around 0.3 to 0.8. The rapeseed was growing from 15 cm to 170 cm during the same time. Then, the harvest started from August. Wheat was sowed after harvest and started growing from September onward.

From Figure 23 (e), it can be seen that the alfalfa started grew since April and matured in June when the height of alfalfa was 50 cm. Then, the NDVI value decreases in July because of mowing. It matured again on August which made the NDVI increase to around 0.9.

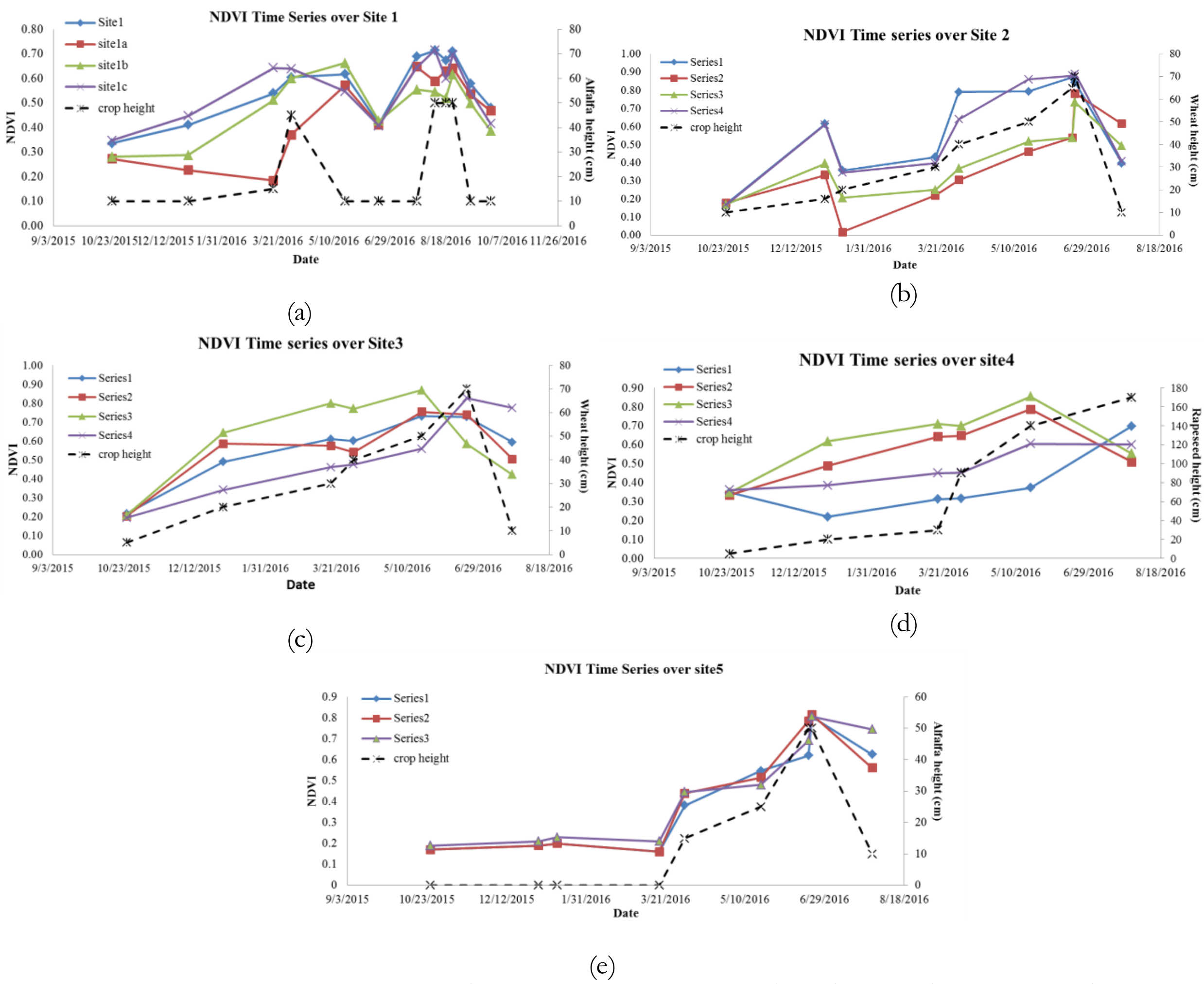

Figure 22 Time series of NDVI and height of alfalfa (a, e) wheat (b) and rapeseed (c) in each field

From the 5 graphs in Figure 23, it can be seen that the NDVI can describe the change of crop height. The regression analysis is made between NDVI over non-inundated area and crop height. The result shows in

Figure 24. The R^2 shows the correlation between NDVI and crop height is quite good, especially in the wheat field (site2). The equation of the regression line was used to estimate the crop height over ponding water during the inundation period in site1 and 2. The result shows in Table 5.

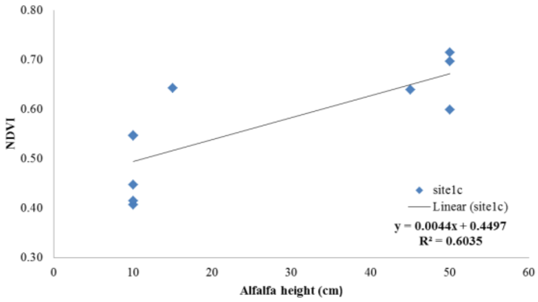

(a)

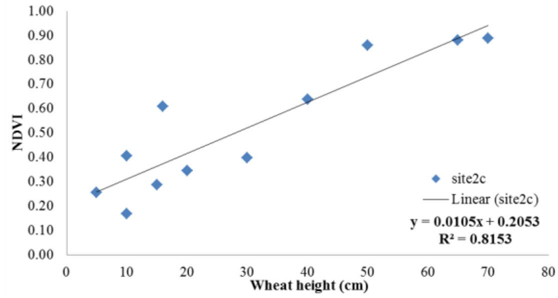

(b)

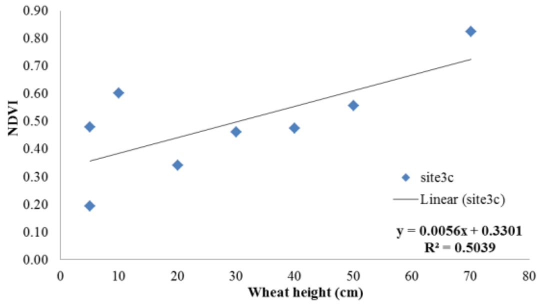

(c)

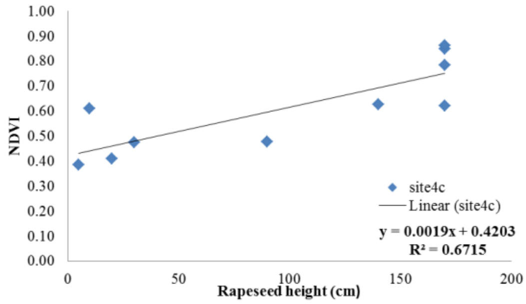

(d)

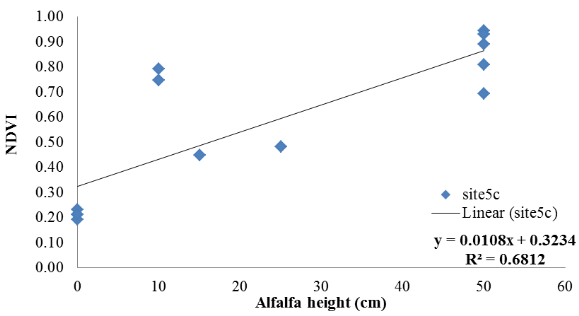

(e)

Figure 23 Relation between NDVI and crop height

The crop height data was collected from the local farmer. Since the crop height was defined by estimation, the accuracy of data cannot be guaranteed. The NDVI was calculated from optical satellite images. Because of the influence from cloud cover, the amount of NDVI data is limited. So, the regression equation is also not very accurate and requires more cloud-free observations to improve. For example, site 1 needs more NDVI value for the crop which has the height of 20-40cm. But the estimated crop height can still be used to show the existence of ponding water. From Table 5, it can be seen that the height of alfalfa in site 1a and 1b is much shorter than the alfalfa in site 1c. Especially in January, March and April, the ponding water nearly covered up the whole alfalfa in site 1a. For site 1b, ponding water covered up the whole alfalfa in January. In March and April, the estimate height is shorter than the normal height. Normally, the alfalfa reaches 45cm in April and then harvest. But the alfalfa in site1b delayed to reach 46 cm in May. The estimate height of wheat in site 2 can also show the influence of ponding water on crop. The whole wheat was covered by the ponding water in January. Then in March, the estimated height is just 1.34cm and 4.20cm. It means that only part of the wheat was above the ponding water. After the inundation period, the crop height in site 2a and 2b is much shorter. It shows that the ponding water can affects and destroy the growth of crop.

Table 5 Estimate crop height over inundated area

	Crop height (cm)						
Date	**Site1a**	**Site1b**	**Site1c**	**Date**	**Site2a**	**Site2b**	**Site2c**
1/1/2016	0	0	10	1/1/2016	12	18	16
3/17/2016	0	11	15	1/13/2016	0	0	20
4/2/2016	0	29	45	3/17/2016	1	4	30
5/20/2016	27	46	10	4/2/2016	9	15	40
6/19/2016	0	0	10	5/20/2016	24	29	50
7/23/2016	44	25	10	6/19/2016	31	31	65
8/8/2016	31	32	50	6/21/2016	54	50	70
8/18/2016	41	24	50	7/23/2016	38	27	10
8/24/2016	43	36	50	8/18/2016	7	7	15

*the negative value is replaced by 0

5.2.2. NDVI and polarization ratio

The ponding water on southern study area can also be identified by using NDVI time series. The NDVI value decreases when ponding water covers the field. In Figure 25, the NDVI of site 1a decreases and stays at around 0.2 from January to March. But at the same time, the NDVI of site1c is 0.5-0.6. The decrease also shows on the NDVI time series of site2a. The NDVI decreases from 0.34 to 0.23 since the end of February. The low NDVI value can also be found over site4. The NDVI of site 4b is around 0.44 which is much lower than the value of site 4c (around 0.7). But from Figure 25 (c), it can be found the there is no difference between time series of site 3, 3a and 3b. So, the ponding water was in test site 1, 2 and 4 from January to March.

The crop information is not available for the southern study area. The polarization ratio was used to compare with NDVI time series. From Figure 25, it can be seen that the trend of NDVI time series matches the change of polarization ratio. In Figure 25 (a, b and d), the peak of polarization ratio is around June when the NDVI also reaches its peak value. In Figure 25 (c), the peak of polarization moves to July when the NDVI reaches its peak value the same time.

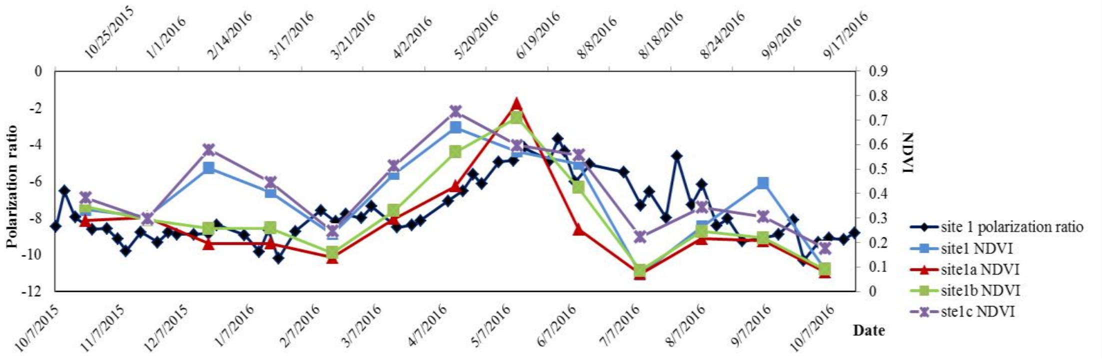
Polarization ratio
NDVI
Date
site 1 polarization ratio
site1 NDVI
site1a NDVI
site1b NDVI
ste1c NDVI

(a)

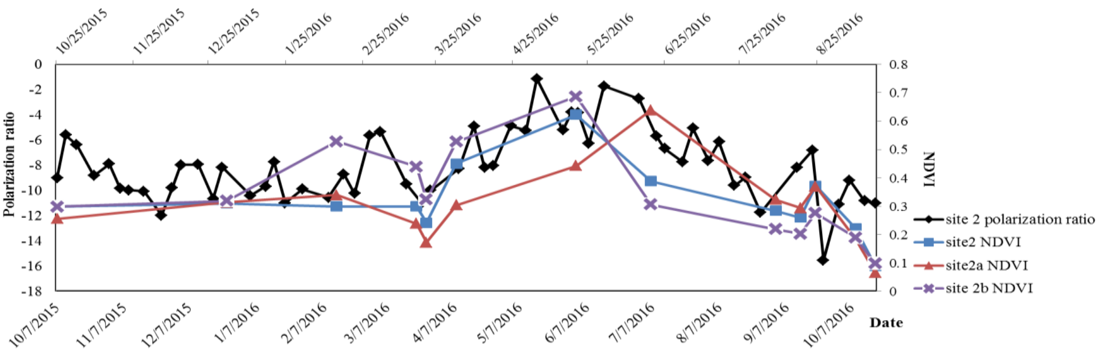
Polarization ratio
NDVI
Date
site 2 polarization ratio
site2 NDVI
site2a NDVI
site 2b NDVI

(b)

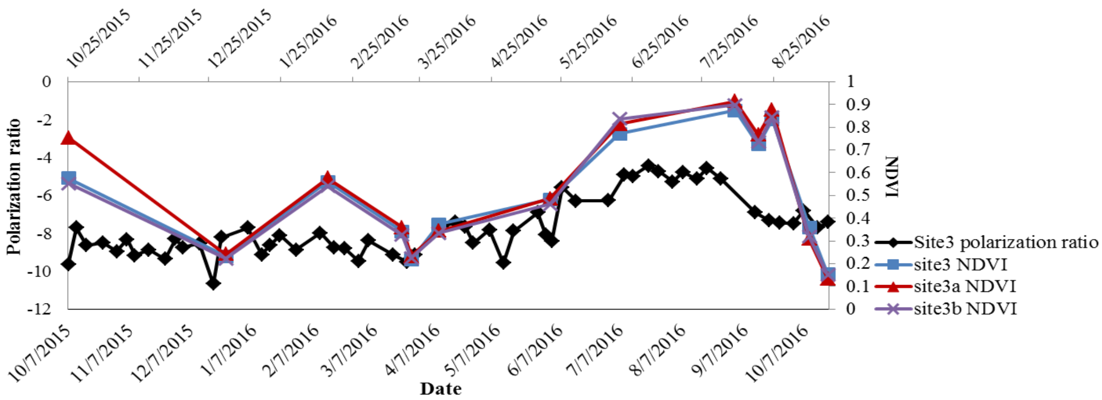
Polarization ratio
NDVI
Date
Site3 polarization ratio
site3 NDVI
site3a NDVI
site3b NDVI

(c)

.

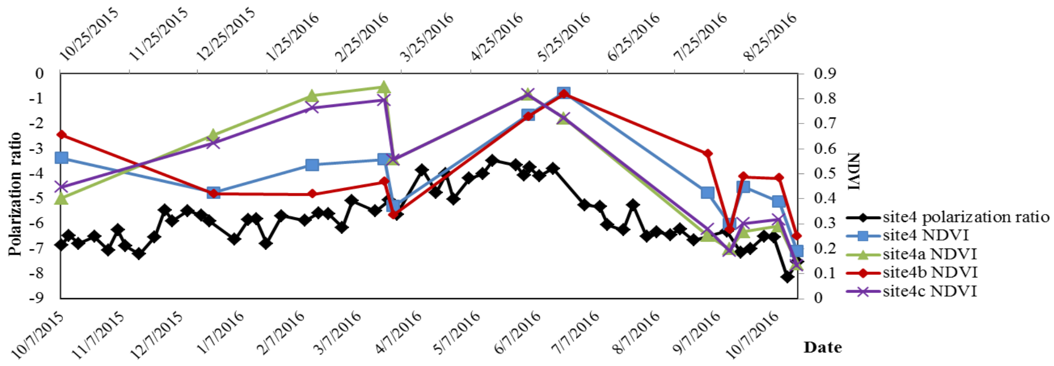

(d)

Figure 24 Time series of NDVI and polarization ratio

The correlation analysis was taken between NDVI and polarization ratio. The R^2 was calculated and shown in Table 6. All the R^2 is larger than 0.6. Among them, the northern test site 2 and southern test 1 has a higher R^2 which is 0.77 and 0.80 respectively. So, the polarization can be used for monitoring the crop growth condition.

Table 6 Relationship between NDVI and polarization ratio

R^2	Test site1	Test site2	Test site3	Test site4	Test site5
North Study area	0.61	0.77	0.64	0.64	0.63
South Study area	0.80	0.60	0.60	0.74	No data

In the NDVI time series, the non-inundated area usually has a higher NDVI value. The NDVI differences between inundated area and non-inundated area were calculated. The differences of polarization ratio were also calculated and compared with the NDVI differences. The result shows in Figure 26. R^2 shows the correlation between the differences of NDVI and polarization ratio. The relation is strong. For southern site 2, the R^2 even reaches 0.84. So, polarization ratio can also be used to display the crop loss caused by ponding water.

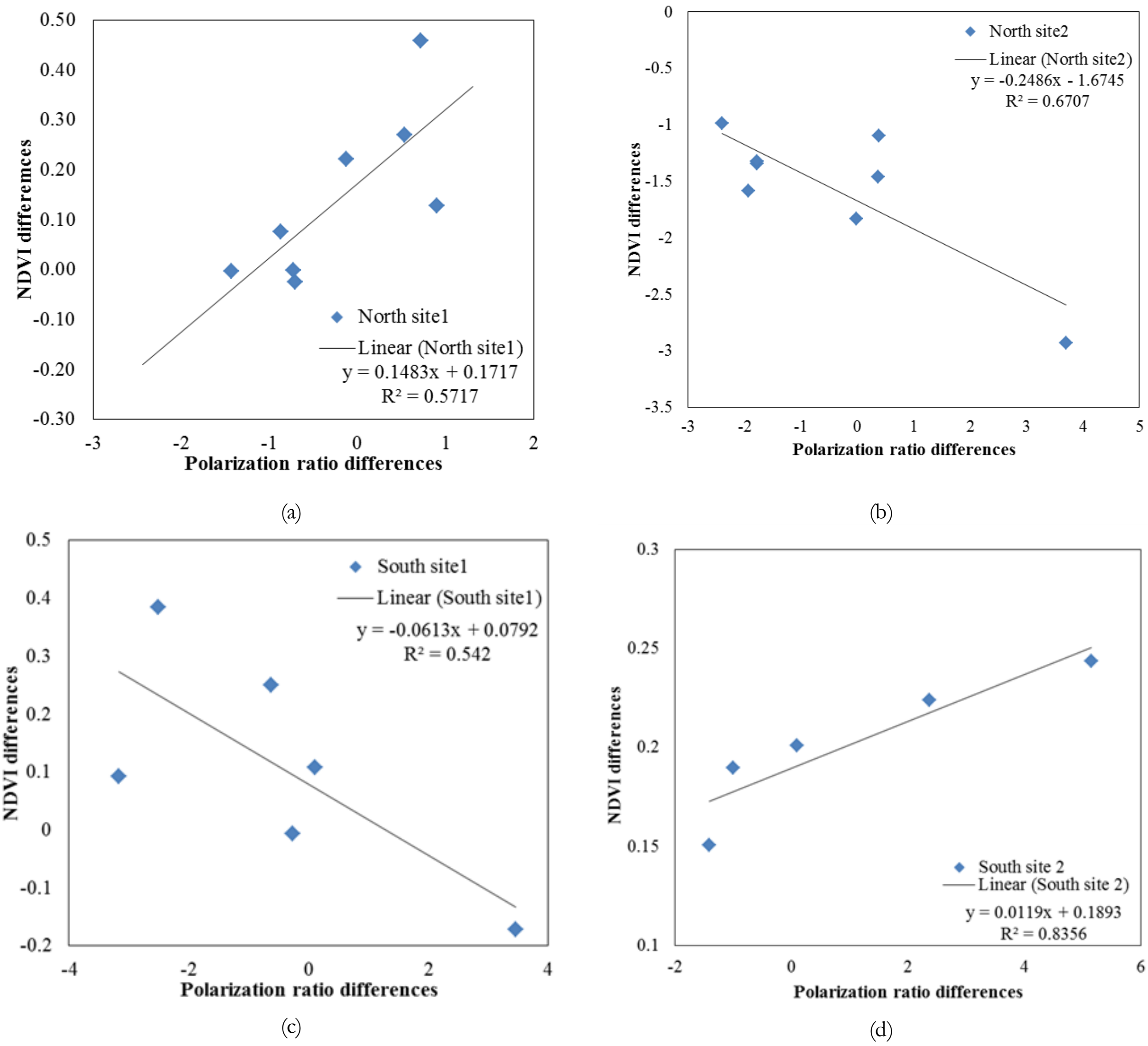

Figure 25 Relationship between NDVI and polarization ratio differences

From the NDVI time series, it can be seen that inundated area has a low NDVI value than non-inundated area. Since ponding water can prevent the crop growth and affect the quantity and quality of agricultural products, so the NDVI difference between inundated area and non-inundated area can be considered proportional to the crop loss. The crop loss rate of NDVI and polarization ratio was calculated and showed in Table 7. Compared with the non-inundated area, NDVI can decreases 71.36% in March in test site1 in the northern region. Polarization ratio changes most on the end of February (about 49.46%). The change rate of NDVI and polarization ratio over site2 is higher than site1. It means the wheat field had more loss than alfalfa field. The wheat is more vulnerable than alfalfa against the ponding water.

Table 7 Crop loss rate estimated by NDVI and polarization ratio

North test site1 (Alfalfa)				**North test site2 (Wheat)**			
Date	**NDVI**	**Date**	**Polarization ratio**	**Date**	**NDVI**	**Date**	**Polarization ratio**
1/1/2016	49.35%	1/4/2016	1.16%	1/1/2016	45.65%	1/4/2016	20.38%

3/17/2016	71.36%	1/11/2016	41.42%	1/13/2016	98.15%	1/11/2016	38.27%
4/2/2016	42.17%	1/23/2016	4.07%	3/17/2016	74.47%	1/15/2016	27.81%
		1/28/2016	26.49%	4/2/2016	63.82%	1/23/2016	12.95%
		2/9/2016	1.11%	5/20/2016	48.34%	2/9/2016	15.46%
		2/16/2016	49.46%			2/16/2016	45.99%
		2/28/2016	42.30%			2/21/2016	1.34%
		3/4/2016	12.41%			2/28/2016	123.14%
		3/11/2016	24.09%			3/16/2016	31.24%
		3/23/2016	17.65%			4/16/2016	50.47%
		3/28/2016	3.80%				
		4/4/2016	9.62%				
		4/16/2016	17.66%				

5.3. Ponding water mapping

5.3.1. Spatial distribution of ponding water

The backscatter time series analysis shows the ponding water can make the backscatter decrease to below -14 dB. This value was used to reclassify the study area for mapping ponding water. A series of Sentinel-1A images were used to map the distribution of ponding water through the whole study period. Figure 27 (a) shows the distribution of ponding water over northern study area from October, 2015 to October, 2016. Permanent water bodies and temporary ponding water was distinguished in the map. Permanent water bodies are in blue and ponding water is in red. The distribution of ponding water in test site 1 and 2 is shown in Figure 27 (b, c). According to the statistic (Table 8), the total area of northern study area is about 2282.66 km². From this, 91.4 km² was affected by the ponding water. It means 4% cropping area was directly affected by the ponding water.

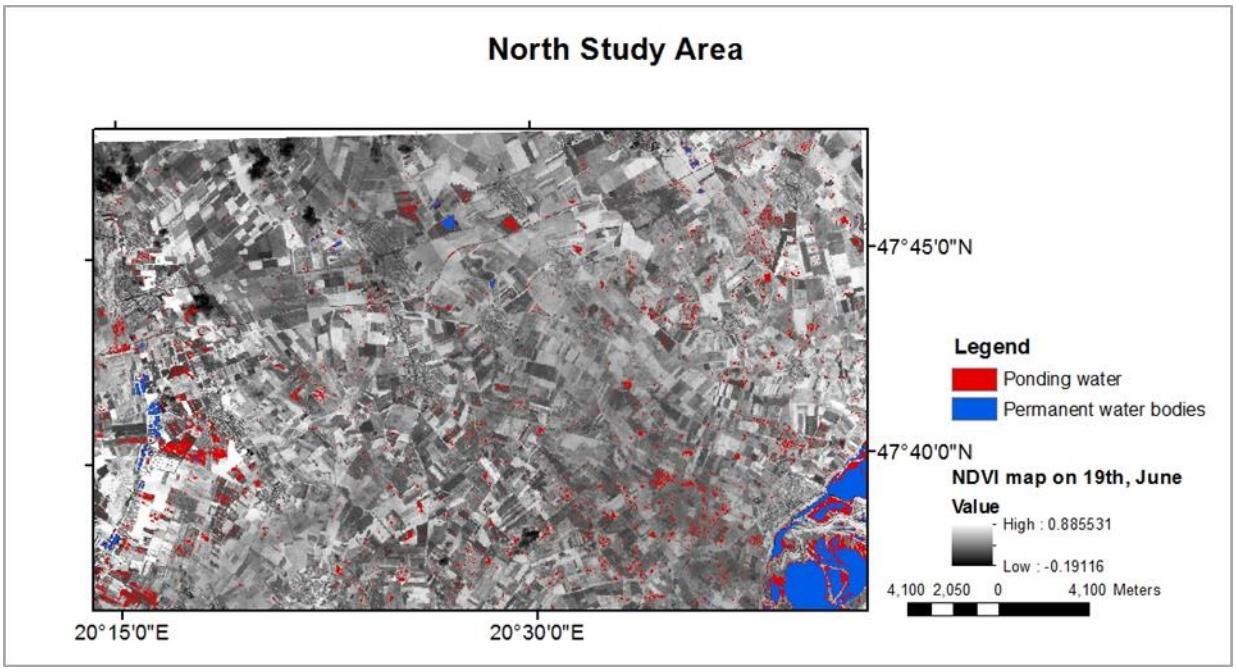

(a)

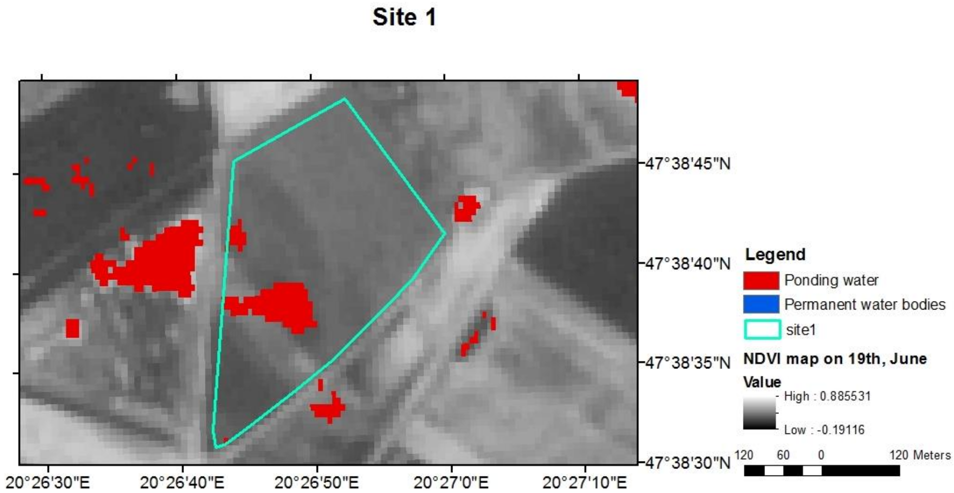

(b)

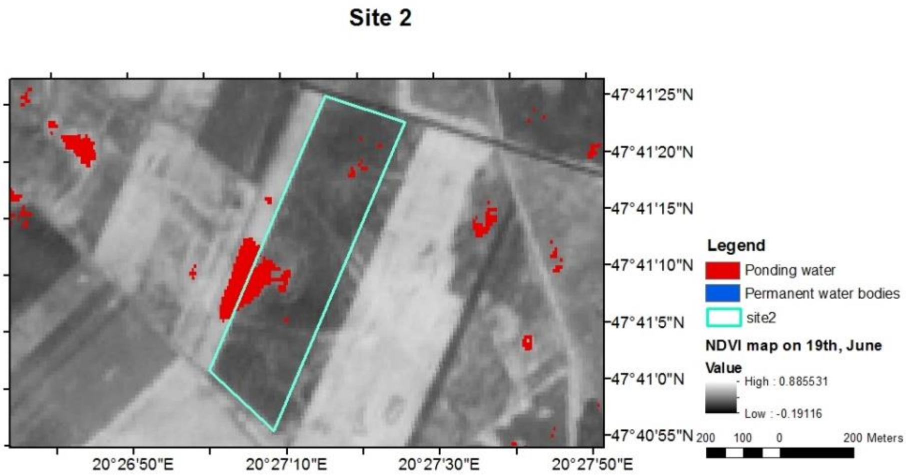

(c)

Figure 26 Spatial distribution of ponding water on northern study area

A similar spatial analysis was also done over the southern study area. The result is shown in Figure 28 (a). The rivers and artificial ponds are in blue. The ponding water is in red. The distribution of ponding water in southern site 1 and 2 is shown in Figure 28 (b and c). The statistic in Table 9 shows that the total area of southern study area is 2006.79km². 3.96% agricultural area was directly affected by the ponding water.

Table 8 Affected area statistic

	Northern study area		Southern study area	
	Area(km^2)	Percentage	Area(km^2)	Percentage
Non-inundation area	21601.21	94.63%	1882.12	93.79%
Ponding water	91.40	4.00%	79.51	3.96%

Permanent water bodies	31.14	1.36%	45.16	2.25%
Total area (km^2)	2282.66		2006.79	

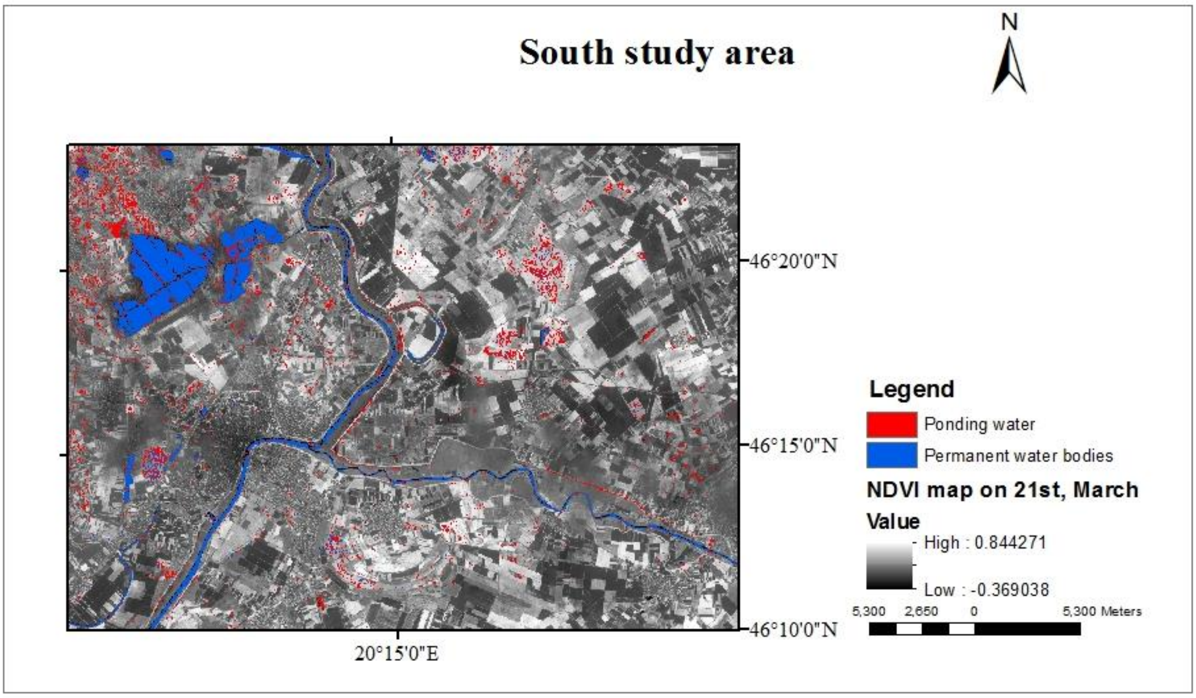

(a)

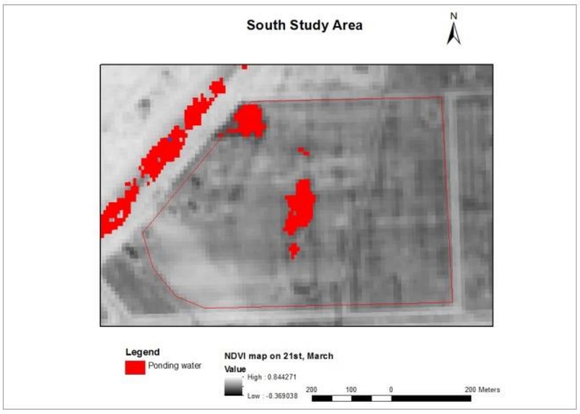

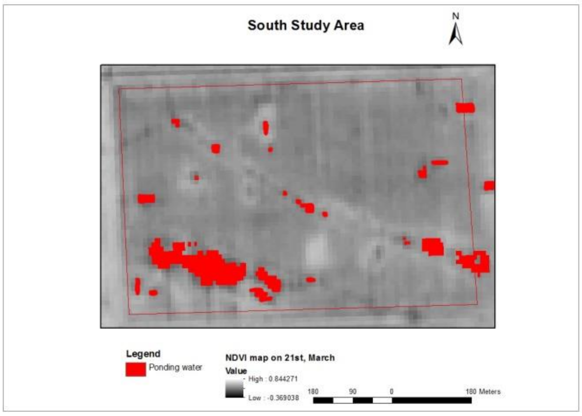

(a) (c)

Figure 27 Spatial distribution of ponding water on southern study area

5.3.2. Temporal distribution of ponding water

In order to see how long the ponding water stay in the field, the temporal inundation distribution map was made. Figure 29 (a) shows the ponding water in northern study area. Figure 29 (b) shows the ponding water on southern study area. The area inundated happened in the different months is show with different colours. Most of the inundation happened in January, February and March. In northern study area, ponding water still existed in April. According to the statistic in Table 9, 49.38km² crop field was covered by ponding water in January. The affected area keeps at around 24km² from February to April. In the southern study area, ponding water occurred mostly in February. There was 133.43km² field covered by ponding water.

Table 9 Affected area monthly statistic

	Northern study area (km^2)	Southern study area (km^2)
January	49.38	26.56
February	24.93	133.43
March	24.80	69.13
April	24.83	

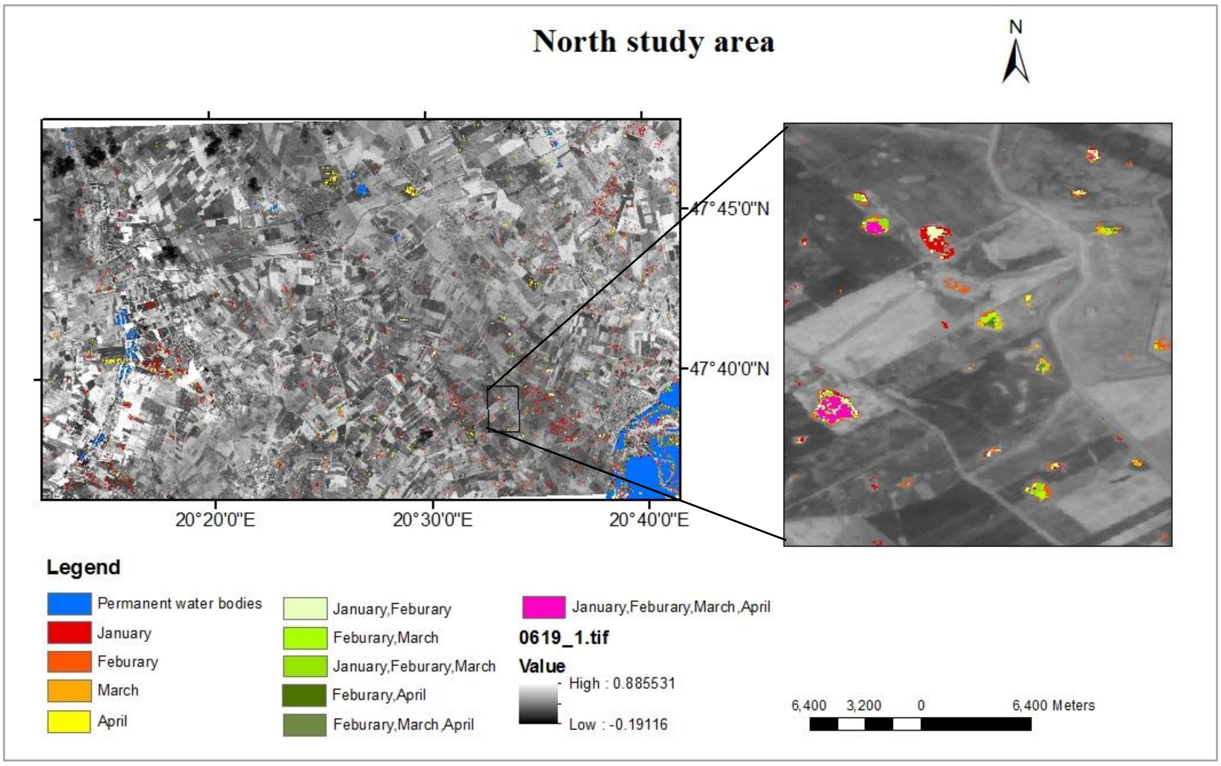

(a)

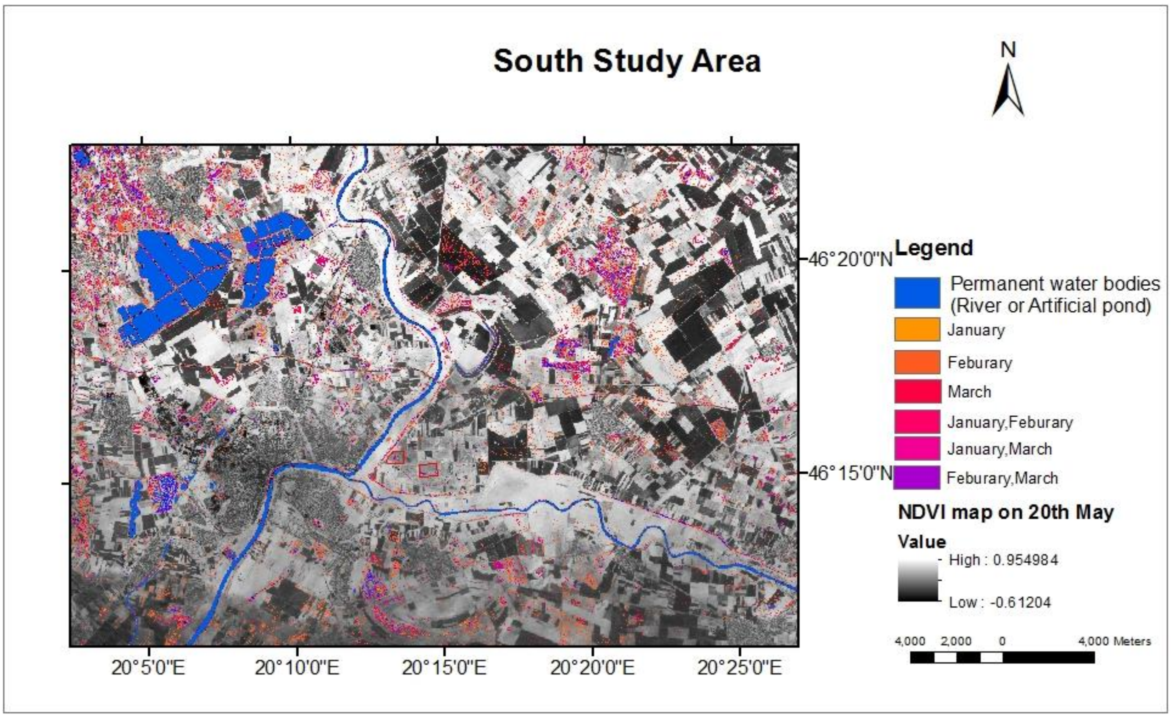

(b)

Figure 28 Temporal distribution of ponding water in northern study area (a) and southern study area (b)

Figure 30 shows the temporal distribution of ponding water over selected test sites. For most of the sites, the crop was affected by the ponding water for over 2 months. For the test sites in the north, the ponding water stayed in the field during from January to February. For the test sites in the south, ponding water stayed in the field from February to March. From Figure 30 (a), it can be seen that there is a big area covered by ponding water. In January, the ponding water occupied the red area and light green area. When it was Februry, the ponding water in light green area was still in the field. The ponding water in orange appeared in the field but the inundation in red disappeared. Figure 30 (b, c, d) can also show the similar dynamic change in other fields.

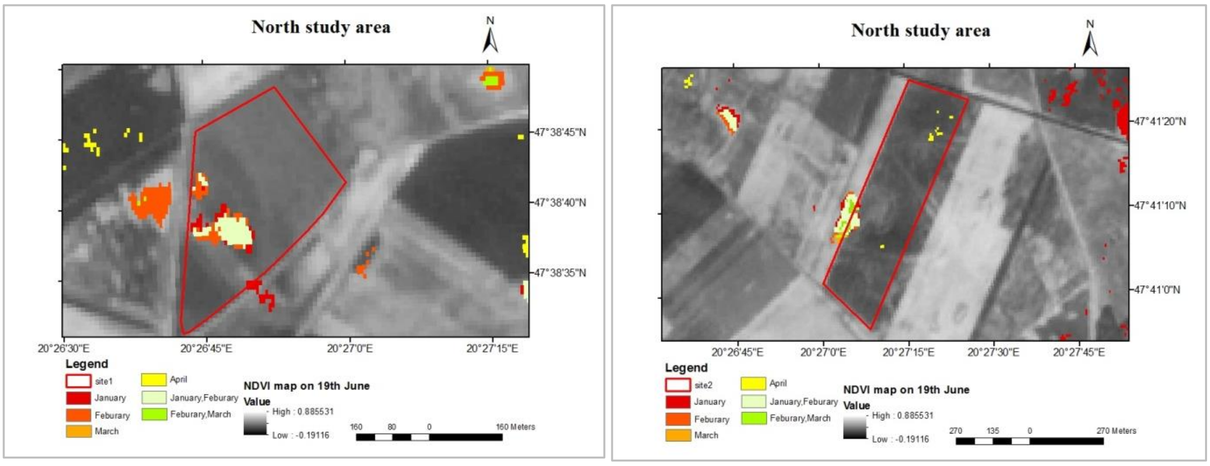

(a) (b)

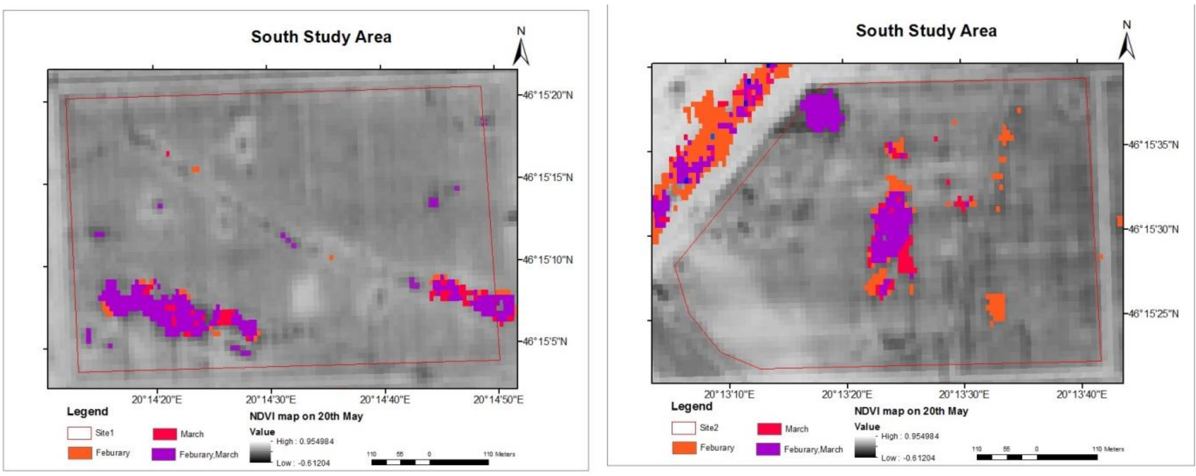

(c) (d)

Figure 29 Temporal distribution of ponding water in some test site

5.3.3. Topography analysis

A about 3.5 cm DEM created from the drone images was used to see if the topography affects the distribution of ponding water. The vertical accuracy of DEM is about 3-4 cm. The DEM of northern site 1 and southern site 4 is shown in Figure 31. From the DEM, it can be seen that the inundation always happens in the lower area. Although the field is nearly flat, there still have some elevation differences and the lower place can accumulate the ponding water easily. From the Figure 31 (a), it can be seen that ponding water happens on the area which is about 87.9 m about above the sea level. It is lower than the area around it. From the Figure 31 (b), the ponding water happens in the area which is about 77.6 m above the sea level. It is also the lower place in the image.

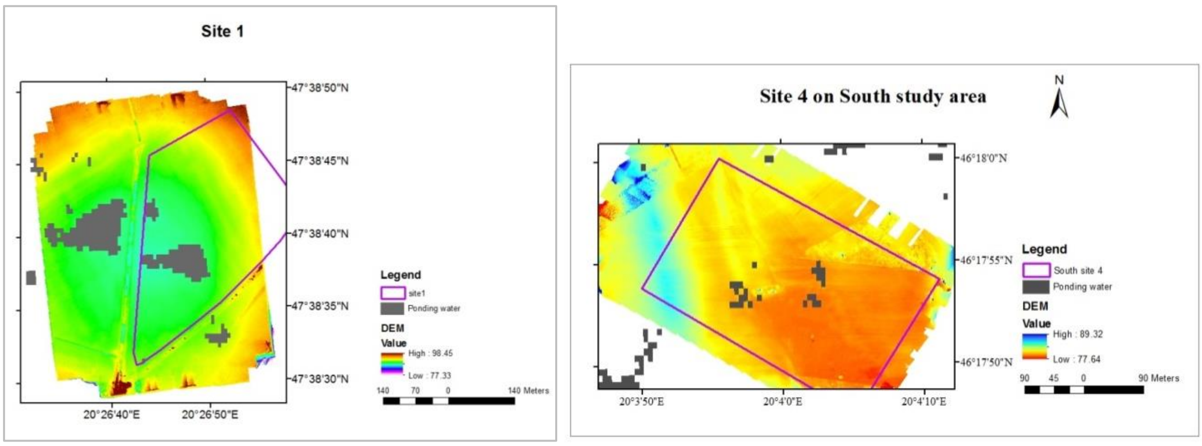

(a) (b)

Figure 30DEM of northern site 1 (a) and southern site 4 (b)

6. CONCLUSION AND RECOMMENDATION

6.1. Conclusion

The objective of this study is to map ponding excess water and assess its effects on crops with Sentinel-1 images, supported by Sentinel-2 images, drone images and field information. A series of Sentinel-1A images were used for detecting ponding water based on the time series analysis of the backscatter. The NDVI time series got from Sentinel-2 images and the polarization ratio time series calculated by Sentinel-1 images was used for monitoring the crop growth condition. Rainfall, soil moisture and NDVI was used as ancillary data for verify the existence of ponding water. Drone images were used for observing the landscape of some test sites and extracting DEM. Five test sites in the northern study area and four test sites in southern study area were analysed. Finally, the spatial and temporal distribution of ponding water was mapped based on the analysis of each test site. This study continues Liu's work (Liu, 2016). In Liu's research, limited number of ponding water could be found in the field. The area of ponding water was smaller than the resolution of Sentinel-1 and could be captured by SAR images. She didn't have the crop information to analyse the time series. All of these limitations are overcome in this study.

The following conclusions are made from the analysis result.

- The area covered by ponding water has a high soil moisture value, and the water accumulated on the surface results in rainfall resulting in a low backscatter value (less than -14 dB). The low backscatter over inundation area is caused by the high specular reflection over smooth water surface.
- Angle correction is a very important step when different incidence angle images are supposed to be used together. The angle correction has to consider the actual conditions of the land cover.
- VV backscatter was used for the time series analysis because it is very sensitive to the soil moisture. The correlation analysis between soil moisture and VV backscatter shows that soil moisture is a dominant factor of backscatter. Rainfall is the driving force of the change of soil moisture. It is also the cause of ponding water. High clay content of the soils leads to the decrease of the infiltration rate which also causes the occurrence of ponding water.
- NDVI can describe the change of crop height. The decrease of NDVI can also help to prove the existence of ponding water in the field. Polarization ratio of radar images can also be used to monitor the crop growth condition because it has a strong correlation with NDVI time series. NDVI and polarization ratio difference between inundation and non-inundation area was calculated and considered as the crop loss. Wheat is found more vulnerable than alfalfa from the crop loss rate calculation.
- About 914km^2 area was affected by ponding water over the northern study area. About 1729 km^2 of southern study area was affected by ponding water. In the northern study area, most of the ponding water stayed in the field from January to February. In the southern study area, most of

the ponding water stayed in the field from February to March. The topography affects the distribution of ponding water.

6.2. Limitations and recommendations

- The angle correction needs more improvement. Although the optimal *n* for different land cover was searched in this study, the SAR images pairs used here for testing the effect of the canopy on *n* were not exactly acquired on the same day and the quantity of images used here was also limited. The optimal *n* values for different land cover types and phonological stages need to be found in the further studies.
- The crop information was collected from a local farm. Some data like crop height is an estimated value. Some analyses were based on this value, so, it affected the corresponding accuracy of estimation in this research.
- More soil moisture data is need for the northern study area to verify the low backscatter results from ponding water. More soil type data is also need to prove how the soil physical properties can affects the ponding water in the further studies.
- In the further studies, the use of polarization ratio needs to be further developed. To define whether polarization ratio can replace NDVI to be an indicator to reflect the coverage of vegetation; its dependence on vegetation growth state and crop phenology is to be studied.

LIST OF REFERENCES

Attema, E., Davidson, M., Floury, N., Levrini, G., Rosich-Tell, B., Rommen, B., & Snoeij, P. (2007). Sentinel-1 ESA's new European SAR mission. Proceedings of S*PIE*, *6744*, 674403-674403–8. https://doi.org/10.1117/12.747146

Bindlish, R., & Barros, A. P. (2001). Parameterization of vegetation backscatter in radar-based , soil moisture estimation. Remote Sensing of Environment, 76, 130–137.

Boni, G., Ferraris, L., Pulvirenti, L., Squicciarino, G., Pierdicca, N., Candela, L., Pagliara, P. (2016). A Prototype System for Flood Monitoring Based on Flood Forecast Combined With COSMO-SkyMed and Sentinel-1 Data. *IEEE* Journal of Selected Topics in Applied Earth Observations and Remote Sensing, 9(6), 2794–2805. https://doi.org/10.1109/JSTARS.2016.2514402

Bozán, C., Körösparti, J., Pásztor, L., Kuti, L., & Pálfai, I. (2013). Mapping of Excess Water Hazard in the Region of South Hungarian Great Plain. In Proceedings of the 13th International Conference on Environmental Science and Technology.

Bruzzone, L., Marconcini, M., Wegmüller, U., & Wiesmann, A. (2004). An advanced system for the automatic classification of multitemporal SAR images. IEEE Transactions on Geoscience and Remote Sensing, 42(6), 1321–1334. https://doi.org/10.1109/TGRS.2004.826821

Brouwer .C. (1988). Annex 2 Infiltration rate and infiltration test. In *Irrigation* Water Management: Irrigation Methods (5th ed.). Retrieved from http://www.fao.org/docrep/S8684E/s8684e0a.htm#annex 2 infiltration rate and infiltration test

Ciampitti, I., Jardine, D., & Diaz, D. R. (2015). Effect of standing water and saturated soils on corn growth and yield. Retrieved from http://www.agprofessional.com/news/effect-standing-water-and-saturated-soils-corn-growth-and-yield

Desnos, Y. L., Buck, C., Guijarro, J., Suchail, J. L., Torres, R., & Attema, E. (2000). ASAR - Envisat's Advanced Synthetic Aperture Radar - Building on ERS achievements towards future earth watch missions. *ESA Bulletin*, (102), 91–100. Retrieved from http://www.esa.int/esapub/bulletin/bullet102/Desnos102.pdf

ESA. (2016a). Level-1C algorithm. Retrieved from https://sentinel.esa.int/web/sentinel/technicalguides/%0Asentinel-2-msi/level-1c/algorithm

ESA. (2016b). Sentinel-1 - ESA EO Missions - Earth Online - ESA. Retrieved May 20, 2016, from https://earth.esa.int/web/guest/missions/esa-operational-eo-missions/sentinel-1

ESA. (2016c). Sentinel-2 - ESA Operational EO Missions - Earth Online - ESA. Retrieved from https://sentinel.esa.int/web/sentinel/missions/sentinel-2

Frulla, L. a., Milovich, J. a., Karszenbaum, H., & Gagliardini, D. a. (1998). Radiometric corrections and calibration of SAR images. IGARSS '98. Sensing and Managing the Environment. 1998 IEEE International Geoscience and Remote Sensing. Symposium Proceedings. (Cat. No.98CH36174), 2(1414), 1147–1149. https://doi.org/10.1109/IGARSS.1998.699700

Gauthier, Y., Bernier, M., & Fortin, J.-P. (1998). Aspect and incidence angle sensitivity in ERS-1 SAR data. International Journal of Remote Sensing, 19(10), 2001–2006. https://doi.org/10.1080/014311698215117

Gstaiger, V., Huth, J., Gebhardt, S., Wehrmann, T., & Kuenzer, C. (2012). Multi-sensoral and automated derivation of inundated areas using TerraSAR-X and ENVISAT ASAR data. International Journal of Remote Sensing, 33(22), 7291–7304. https://doi.org/10.1080/01431161.2012.700421

Guerschman, J. P., Warren, G., Byrne, G., Lymburner, L., Mueller, N., & Dijk, A. Van. (2011). MODIS-based standing water detection for flood and large reservoir mapping: algorithm development and applications for the Australian continent. Www.Csiro.Au. Retrieved from http://www.clw.csiro.au/publications/waterforahealthycountry/wirada/TechReports/WIRADA-MODIS-standing-water.pdf

Mucsi, L., & Henits, L. (2016). Creating excess water iundation maps by sub-pixel classification of medium. Environmental Geography, 3 No.1-4(August), 31–40.

Ho, J., Ryu, D., Costelloe, J., Chan, F., Marinova, D., & Anderssen, R. S. (2011). Comparative Analysis of NDVI and Microwave-Derived Soil Moisture for Determining Surface Water in the Cooper Creek Catchment. 19th International Congress on Modelling and Simulation (Modsim2011), (December), 1951–1958.

Hoque, R., Nakayama, D., Matsuyama, H., & Matsumoto, J. (2011). Flood monitoring, mapping and assessing capabilities using RADARSAT remote sensing, GIS and ground data for Bangladesh.

Natural Hazards, *57*(2), 525–548. https://doi.org/10.1007/s11069-010-9638-y
ITC. (2016). ITC database of satellites and sensors. Retrieved from https://www.itc.nl/Pub/sensordb/AllSatellites.aspx
Jeyaseelan, A. T. (2003). Droughts & floods assessment and monitoring using remote sensing and GIS. *Satellite Remote Sensing and GIS* Applications in Agricultural Meteorology, 291–313. Retrieved from http://www.wamis.org/agm/pubs/agm8/Paper-14.pdf
Jiao, X., McNairn, H., Shang, J., Pattey, E., Liu, J., & Champagne, C. (2009). The sensitivity of RADARSAT-2 quad-polarization SAR data to crop LAI. Remote Sensing and Modeling of Ecosystems for Sustainability, *7454*(August 2016), 74540O–74540O–11. https://doi.org/10.1117/12.825701
Joyce, K. E., Belliss, S. E., Samsonov, S. V., McNeill, S. J., & Glassey, P. J. (2009). A review of the status of satellite remote sensing and image processing techniques for mapping natural hazards and disasters. Progress in Physical Geography*, 33(2), 18*3–207. https://doi.org/10.1177/0309133309339563
Karoly, B., Teodora, B., Balazs, B., & Brikic, M. (2013). *INLAND EXCESS WATER*. Szegedi Tudományegyetem TTIK Természeti Földrajzi és Geoinformatikai Tanszék. Retrieved from http://jlevente.com/publications/SzatmariVanLeeuwen_Inland_Excess_Water.pdf
Kuti, L., Kerék, B., & Vatai, J. (2006). Problem and Prognosis of Excess Water, Geological Institute of Hungary, *1*(1), 5–18.
La, S., Del, B., & Hamsom, M. (1987). Understanding the Normalized Difference Vegetation Index. Physical Oceanography, (1), 2–5.
Lantzanakis, G., Mitraka, Z., & Chrysoulakis, N. (2017). Perspectives on Atmospheric Sciences, 255–261. https://doi.org/10.1007/978-3-319-35095-0
Leeuwen, B. Van, Henits, L., Mészáros, M., Tobak, Z., Szatmári, J., Pavić, D., … Dolinaj, D. (2013). Classification Methods for Inland Excess Water Modeling. Journal of Environmental Geography, *6*, 1–8. https://doi.org/10.2478/v10326-012-0001-5
Leeuwen, B. Van, & Tobak, Z. (2014). Operational Identification of Inland Excess Water Floods Using Satellite Imagery. GI_Forum 2014 – Geospatial Innovation for Society, (August), 12–15. https://doi.org/10.1553/giscience2014s12.Operational
Lenney, M. P., Woodcock, C. E., Collins, J. B., & Hamdi, H. (1996). The status of agricultural lands in Egypt: The use of multitemporal NDVI features derived from landsat TM. Remote Sensing of Environment, 56(1), 8–20. https://doi.org/10.1016/0034-4257(95)00152-2
LingFang Zeng, Lin Li, L. W. (2015). SAR-based Fast Flood Mapping Using Sentinel-1 Imagery. Geomtics world, *22*(5), 100–107. Retrieved from http://www.airitilibrary.com/Publication/alDetailedMesh?docid=dlxxsj201505020
Liu, C. (2016). Analysis of Sentinel-1 SAR data for mapping standing water in the Twente region. MSC thesis. Retrieved from www.itc.nl/library/papers_2016/msc/wrem/cliu.pdf
Mezosi, G., Bata, T., Meyer, B. C., Blanka, V., & Ladanyi, Z. (2014). Climate Change Impacts on Environmental Hazards on the Great Hungarian Plain, Carpathian Basin. International Journal of Disaster Risk Science, 5(2), 136–146. https://doi.org/10.1007/s13753-014-0016-3
Mikl, C. Z. (2011). Outline of floods as well as flood prevention and flood protection activities in Hungary. Technology, 10(1), 123–129.
Moran, S. M., Alonso, L., Moreno, J. F., Cendrero Mateo, M. P., De La Cruz, F. D., & Montoro, A. (2012). A RADARSAT-2 quad-polarized time series for monitoring crop and soil conditions in Barrax, Spain. IEEE Transactions on Geoscience and Remote Sensing, 50(4), 1057–1070. https://doi.org/10.1109/TGRS.2011.2166080
O'Grady, D., Leblanc, M., & Gillieson, D. (2013). Relationship of local incidence angle with satellite radar backscatter for different surface conditions. International Journal of Applied Earth Observation and Geoinformation, *24*(1), 42–53. https://doi.org/10.1016/j.jag.2013.02.005
Paloscia, S., Pettinato, S., Santi, E., Notarnicola, C., Pasolli, L., & Reppucci, A. (2013a). Soil moisture mapping using Sentinel-1 images: Algorithm and preliminary validation. Remote Sensing of Environment, 134, 234–248. https://doi.org/10.1016/j.rse.2013.02.027
Paloscia, S., Pettinato, S., Santi, E., Notarnicola, C., Pasolli, L., & Reppucci, A. (2013b). Soil moisture mapping using Sentinel-1 images: Algorithm and preliminary validation. Remote Sensing of Environment, 134, 234–248. https://doi.org/10.1016/j.rse.2013.02.027
Pásztor, L., Körösparti, J., Bozán, C., Laborczi, A., & Takács, K. (2014). Spatial risk assessment of hydrological extremities: Inland excess water hazard, Szabolcs-Szatmár-Bereg County, Hungary.

Journal of Maps, 5647(September), 1–9. https://doi.org/10.1080/17445647.2014.954647
Pierdicca, N., Chini, M., Pulvirenti, L., Candela, L., Ferrazzoli, P., Guerriero, L., & Boni, G. (2009). Using Cosmo-Skymed data for flood mapping: some case-studies. *2009 IEEE* International Geoscience and Remote Sensing Symposium, *2*, II-933.
Rauste, Y., Lönnqvist, A., Molinier, M., Henry, J., & Häme, T. (2007). Ortho-Rectification and Terrain Correction of Polarimetric SAR Data Applied in the ALOS / Palsar Context. *Methods*, (August 2016), 1618–1621.
Rouse, J. W., Haas, R. H., Schell, J. A., & Deering, D. W. (1973). Monitoring vegetation systems in the Great Plains with ERTS. In & M. A. B. S. C. Freden, E. P. Mercanti (Ed.), Third Earth resources technology satellite-1 symposium (Vol. 1, pp. 309–317). Washington, United States: NASA. Retrieved from http://ntrs.nasa.gov/archive/nasa/casi.ntrs.nasa.gov/19740022592.pdf
Schlaffer, S., Matgen, P., Hollaus, M., & Wagner, W. (2015). Flood detection from multi-temporal SAR data using harmonic analysis and change detection. International Journal of Applied Earth Observation and Geoinformation, *38*, 15–24. https://doi.org/10.1016/j.jag.2014.12.001
Skakun, S. (2012). The use of time-series of satellite data to flood risk mapping. International Journal Information Models and Analyses, *1*, 260–270.
Torres, R., Snoeij, P., Geudtner, D., Bibby, D., Davidson, M., Attema, E., … Rostan, F. (2012). GMES Sentinel-1 mission. Remote Sensing of Environment, *120*, 9–24. https://doi.org/10.1016/j.rse.2011.05.028
Twele, A., Cao, W., Plank, S., & Martinis, S. (2016). Sentinel-1-based flood mapping: a fully automated processing chain. International Journal of Remote Sensing, *37*(13), 2990–3004. https://doi.org/10.1080/01431161.2016.1192304
Van der Velde, R.. (2010). Soil moisture remote sensing using active microwaves and land surface modeling. Ph. D. Thesis. Retrieved from http://itc.nl/library/papers_2010/phd/vd_velde.pdf
Van der Velde, R., Salama, M. S., Eweys, O. A., Wen, J., & Wang, Q. (2014). Active / Passive Microwave Observations Over the East of the Netherlands. *IEEE* Journal of Selected Topics in Applied Eath Observation and Remotesensing, 8(9), 1–18.
Wardlow, B. D., & Egbert, S. L. (2008). Large-area crop mapping using time-series MODIS 250m NDVI data: An assessment for the U.S. Central Great Plains. Remote Sensing of Environment, 1*12*(3), 1096–1116. https://doi.org/10.1016/j.rse.2007.07.019
Wardlow, B. D., Egbert, S. L., & Kastens, J. H. (2007). Analysis of time-series MODIS 250m vegetation index data for crop classification in the U.S. Central Great Pla*ins. Remote Sensing of Environment, 108*(3), 290–310. https://doi.org/10.1016/j.rse.2006.11.021
Xie, Y., Sha, Z., & Yu, M. (2008). Remote sensing imagery in vegetation mapping: a review. Journal of Plant Ecology-Uk, 1(1), 9–23. https://doi.org/10.1093/jpe/rtm005
Zribi, M., Baghdadi, N., Holah, N., & Fafin, O. (2005). New methodology for soil surface moisture estimation and its application to ENVISAT-ASAR multi-incidence data inversion, *96*, 485–496. https://doi.org/10.1016/j.rse.2005.04.005

APPENDIX 1

			2015			2016									
	soil type (sand%/silt%/clay%)		Oct	Nov	Dec	Jan	Feb	Mar	Apr	May	Jun	Jul	Aug	Sep	Oct
field 1	KA= 42	height of crop (cm)	10	10	10	10	10	15	45	10	10	10	50	10	10
		type	alfalfa												
		agricultural activity	"growing"							mowing	"growing"	mowing	"growing"	mowing	
field2	KA= 44	height of crop (cm)	5	10	16	20	20	30	40	50	65-70	10	5	15	20
		type	wheat										rape		
		agricultural activity	sowing	"growing"								harvest	sowing	"growing"	
field3	KA= 42	height of crop (cm)	5	10	14	20	22-25	30	40	50	65-70	10	5	15	20
		type	wheat										rape		
		agricultural activity	sowing	"growing"								harvest	sowing	"growing"	
field4	KA= 43	height of crop (cm)	5	15	20	20	20	30	90-100	140	170	170	10	10	15
		type	rape										wheat		
		agricultural activity	sowing	"growing"								harvest		sowing	
field5	KA= 44	height of crop(cm)							15	25	50	10	50	10	10
		type	plough						alfalfa						
		agricultural activity										mowing	"growing"		

KA= the property of clay (%)

APPENDIX 2

Production detail about Sentinel-2 (ITC, 2016)

Band of Sentinel-2 images	**Wavelength (µm)**	**Bandwidth (µm)**	**Resolution (m)**	**Swath width (km)**	**Revisit time (days)**
Band1 Coastal/Aerosol	0.443	0.02	60	290	5
Band2 Blue (VIS)	0.49	0.065	10	290	5
Band3 Green (VIS)	0.56	0.035	10	290	5
Band4 Red (VIS)	0.665	0.03	10	290	5
Band5 (VIS)	0.705	0.015	20	290	5
Band6 (VIS)	0.74	0.015	20	290	5
Band7 (VIS)	0.775	0.02	20	290	5
Band8 Near Infrared	0.842	0.115	10	290	5
Band8a Near Infrared	0.865	0.02	20	290	5
Band9 Near Infrared	0.94	0.02	60	290	5
Band10 SWIR	1.375	0.02	60	290	5
Band11 SWIR	1.61	0.09	20	290	5
Band12 SWIR	2.19	0.18	20	290	5

Production detail about Landsat 8 (ITC, 2016)

Band of Landsat8 images	**Wavelength (µm)**	**Resolution (m)**	**Swath width (km)**
Band1 Coastal/Aerosol	0.43 to0.45	30	185
Band2 Blue (VIS)	0.45 to 0.51	30	185
Band3 Green (VIS)	0.53 to 0.59	30	185
Band4 Red (VIS)	0.64 to 0.67	30	185
Band5 Near Infrared	0.85 to 0.88	30	185
Band6 SWIR1	1.57 to 1.65	30	185
Band7 SWIR2	2.11 to 2.29	30	185
Band8 Panchromatic	0.5 to 0.68	15	185
Band9 Cirrus	1.36 to 1.38	30	185